Major Thesis (1).docx

Indian Institute of Science Education and Research, Berhampur

Document Details

Submission ID
trn:oid:::3618:140796939

Submission Date
May 28, 2026, 5:31 PM GMT+5:30

Download Date
May 28, 2026, 5:41 PM GMT+5:30

File Name
Major Thesis (1).docx

File Size
3.2 MB

70 Pages

20,617 Words

114,839 Characters

7% Overall Similarity

The combined total of all matches, including overlapping sources, for each database.

Filtered from the Report

- Bibliography
- Small Matches (less than 10 words)

Match Groups

82 Not Cited or Quoted 7%
Matches with neither in-text citation nor quotation marks

0 Missing Quotations 0%
Matches that are still very similar to source material

0 Missing Citation 0%
Matches that have quotation marks, but no in-text citation

0 Cited and Quoted 0%
Matches with in-text citation present, but no quotation marks

Top Sources

5% Internet sources
4% Publications
3% Submitted works (Student Papers)

Integrity Flags

0 Integrity Flags for Review

No suspicious text manipulations found.

Our system's algorithms look deeply at a document for any inconsistencies that would set it apart from a normal submission. If we notice something strange, we flag it for you to review.

A Flag is not necessarily an indicator of a problem. However, we'd recommend you focus your attention there for further review.

Match Groups

- **82** Not Cited or Quoted 7%
  Matches with neither in-text citation nor quotation marks
- **0** Missing Quotations 0%
  Matches that are still very similar to source material
- **0** Missing Citation 0%
  Matches that have quotation marks, but no in-text citation
- **0** Cited and Quoted 0%
  Matches with in-text citation present, but no quotation marks

Top Sources

5% Internet sources
4% Publications
3% Submitted works (Student Papers)

Top Sources

The sources with the highest number of matches within the submission. Overlapping sources will not be displayed.

1	Internet	dspace.dtu.ac.in:8080 — 2%
2	Publication	F. Ungan, M.E. Mora-Ramos, M.G. Barseghyan, L.M. Pérez, D. Laroze. "Intersubba... — <1%
3	Internet	acikerisim.cumhuriyet.edu.tr — <1%
4	Publication	Cleverson Filgueiras, Moises Rojas, Vinicius T. Pieve, Edilberto O. Silva. "Impact of ... — <1%
5	Submitted works	Delhi Technological University on 2026-05-19 — <1%
6	Publication	A. Turker Tuzemen, H. Dakhlaoui, M.E. Mora-Ramos, E.B. Al, F. Ungan. "Nonlinear ... — <1%
7	Submitted works	Higher Education Commission Pakistan on 2015-10-12 — <1%
8	Internet	d-nb.info — <1%
9	Internet	www.ukessays.com — <1%
10	Internet	link.springer.com — <1%

11 Publication
R. Boussetta, O. Mommadi, M. Hbibi, S. Chouef, A. El Moussaouy, C.A. Duque, A. K... <1%

12 Submitted works
Maharshi Dayanand University on 2017-04-15 <1%

13 Internet
ia601303.us.archive.org <1%

14 Publication
John P. Dakin, Robert G. W. Brown. "Handbook of Optoelectronics - Concepts, Dev... <1%

15 Publication
S. Sakiroglu, H. Sari. "Contribution of the impurity to the thermodynamic properti... <1%

16 Internet
poornaprajnapublication.com <1%

17 Publication
T.V. Diffo, A.J. Fotue, S.C. Kenfack, R.M. Keumo Tsiaze, E. Baloitcha, M.N. Hounkon... <1%

18 Internet
staff.washington.edu <1%

19 Publication
A. B. Davlatov, A. H. Hameed, K. Feddi, P. J. Baymatov et al. "Strain, pressure and t... <1%

20 Publication
L.G. Lafaurie, Y.A. Suaza, D. Laroze, W. Gutiérrez, J.H. Marín. "Thermodynamic pro... <1%

21 Submitted works
National University of Ireland, Galway on 2012-11-06 <1%

22 Internet
www.aerosols.eas.gatech.edu <1%

23 Internet
www.nature.com <1%

24 Internet
coek.info <1%

25 Internet
digital.library.unt.edu <1%

26 Publication
M. Sayrac, A. Turkoglu, M. E. Mora-Ramos, F. Ungan. "Intensity-dependent nonlin... <1%

27 Publication
Richart E. Slusher, Gadi Lenz, Juan Hodelin, Jasbinder Sanghera, L. Brandon Shaw,... <1%

28 Publication
S. Y. López, M. E. Mora-Ramos, C. A. Duque. "Nonlinear optical absorption and opt... <1%

29 Submitted works
University of Birmingham on 2019-03-29 <1%

30 Submitted works
University of Sheffield on 2024-03-28 <1%

31 Internet
dokumen.pub <1%

32 Internet
www.isp.nsc.ru <1%

33 Internet
www.researching.cn <1%

34 Internet
www.science.gov <1%

35 Publication
Advanced Photonics with Second-Order Optically Nonlinear Processes, 1998. <1%

36 Publication
B. Akbarnavaz Farkoush, Gh. Safarpour, A. Zamani. "Linear and nonlinear optical ... <1%

37 Publication
Ceng Chang, Xuechao Li, Yiming Duan, Zhang Zhao, Liangcheng Zhang. "Effects o... <1%

38 Publication
F. Büyükkiliç, D. Demirhan. "A statistical mechanical investigation of the pseudo-... <1%

39 Publication

F. Manfouo, M. Silenou, M. F. C. Fobasso, B. Donfack, A. J. Fotue. "Comparative stu... <1%

40 Submitted works

University of Monastir on 2024-08-24 <1%

41 Submitted works

University of Sheffield on 2026-03-31 <1%

42 Internet

aranne5.bgu.ac.il <1%

43 Internet

c.coek.info <1%

44 Internet

getrevising.co.uk <1%

45 Internet

l.xif.fr <1%

46 Internet

www.researchgate.net <1%

47 Publication

"Quantum Well Intersubband Transition Physics and Devices", Springer Nature, 1... <1%

48 Publication

C. Thirstrup. "Refractive index modulation based on excitonic effects in GaInAs-In... <1%

49 Publication

Gül, Dīlara. "Nonlinear Optical Properties of a Two-Dimensional Quantum Pseudo... <1%

50 Publication

K. Lakaal, L.M. Pérez, M. Kria, J. El Hamdaoui, C.O. Edet, V. Prasad, D. Laroze, E. Fe... <1%

51 Publication

Nguyen Quang Hoc, Phan Van Vuong, Tran Le Thien Nhan, Nguyen Dang Quang ... <1%

52 Publication

Oubram, Outmane, Luis Cisneros-Villalobos, Mario Limon-Mendoza, Francisco Aq... <1%

53	Publication	
Yesilgul, U., E.B. Al, J.C. Martínez-Orozco, R.L. Restrepo, M.E. Mora-Ramos, C.A. Du...		<1%
54	Publication	
Zhuang Zhao, Xuechao Li, Yiming Duan, Ceng Chang, Liangcheng Zhang. "Nonlin...		<1%
55	Internet	
acikerisim.aksaray.edu.tr		<1%
56	Internet	
bibliotecadigital.udea.edu.co		<1%
57	Internet	
sid.ir		<1%
58	Internet	
worldwidescience.org		<1%

A DISSERTATION

SUBMITTED IN FULFILLMENT OF THE REQUIREMENTS FOR THE AWARD OF THE DEGREE

OF

MASTERS OF SCIENCE
IN
PHYSICS

Submitted by:
SHIVANGI GUPTA
24/MSCPHY/29
&
NAMAN JAIN
24/MSCPHY/22

Under the supervision of
Prof. RINKU SHARMA

DEPARTMENT OF APPLIED PHYSICS

DELHI TECHNOLOGICAL UNIVERSITY

(Formerly Delhi College of Engineering)

Bawana Road, Delhi – 110042

DEPARTMENT OF APPLIED PHYSICS

DELHI TECHNOLOGICAL UNIVERSITY

(Formerly Delhi College of Engineering)

Bawana road, Delhi – 110042

CANDIDATE'S DECLARATION

We, SHIVANGI GUPTA, Roll No(s). 24/MSCPHY/29 and NAMAN JAIN, 24/MSCPHY/22 students of M.Sc. Physics hereby declares that the project Dissertation titled "Tunable Mid-Infrared Nonlinear Optics in Chalcogenide 1D $As_2(Se_xTe_{1-x})_3$ Step Quantum Wells" which is submitted by us to the Department of Applied Physics, Delhi Technological University, Delhi in fulfilment of the requirement for the award of the degree of Master of Science is original and not copied from any source without proper citation. This work has not previously formed the basis for the award of any Degree, Diploma Associateship, Fellowship or other similar title or recognition.

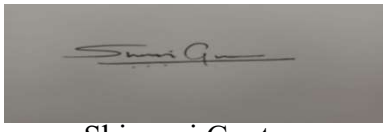

Place: Delhi

Shivangi Gupta

Naman Jain

This is to certify that the student has incorporated all the corrections suggested by the examiners in the thesis and that the statement made by the candidate is correct to the best of our knowledge.

Prof. Rinku Sharma

(Professor, DTU)

DEPARTMENT OF APPLIED PHYSICS
DELHI TECHNOLOGICAL UNIVERSITY
(Formerly Delhi College of Engineering)
Bawana Road, Delhi-110042

CERTIFICATE

I hereby certify that the Project Dissertation titled " Tunable Mid-Infrared Nonlinear Optics in Chalcogenide 1D $As_2(Se_xTe_{1-x})_3$ Step Quantum Wells " which is submitted by SHIVANGI GUPTA, Roll No.(s) 24/MSCPHY/29 and NAMAN JAIN, 24/MSCPHY/22, Department of Applied Physics, Delhi Technological University, Delhi in fulfillment of the requirement for the award of the degree of Master of Science, is a record of the project work carried out by the students under my supervision. To the best of my knowledge this work has not been submitted in part or full for any Degree or Diploma to this University or elsewhere.

Place: Delhi

PROF. RINKU SHARMA
SUPERVISOR

ACKNOWLEDGEMENT

We would like to express our deepest sincere gratitude to our supervisor, Prof. Rinku Sharma, Professor, Department of Applied Physics, Delhi Technological University for giving us the opportunity to work under her guidance and for constant inspiration and incessant support throughout the project. We take this opportunity to express our indebtedness to our supervisor for her enthusiastic help, her expertise, brilliant ideas, valuable suggestions, and constant encouragement. We are grateful to acknowledge the constant help and convenience at every step of our project by our Guest faculty Dr. Priyanka, Dept. of Applied Physics. Lately, we are thankful to our families and friends for their love, care, and support who patiently extended all sorts of help for accomplishing this task.

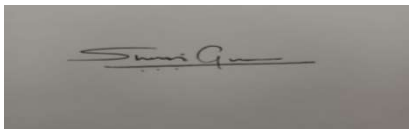

SHIVANGI GUPTA
(24/MSCPHY/29)

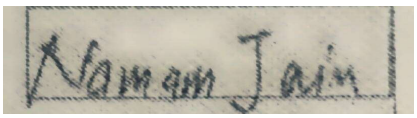

NAMAN JAIN
(24/MSCPHY/22)

ABSTRACT

This dissertation presents a comprehensive computational investigation into the nonlinear optical and thermodynamic properties of stepped quantum well structure. The materials studied here are two low-dimensional materials. The first is a chalcogenide alloy As_2SeTe and second is a two-dimensional MoS_2 monolayer. The study investigates how external fields and material composition change the way these structures interacts with light and thermal energy. To study these interactions we solved one dimensional schrodinger equation using finite element method. We also included Varshini and Kane model in order to see the effects of pressure and temperature on the systems via effective mass. Then we computed the eigenenergies and transition dipole matrices of the system. Then we used these paramters into Density matrix Formulism and canonical partition function to calculated various thermal and optical responses of these systems. We focused to compute linear and nonlinear absorption, refractive index change, second harmonic generation (SHG), and third harmonic generation (THG) for optical studies and Helmholtz free energy, entropy, heat capacity, and the magnetocaloric effect for the thermodynamic studies. This work tries to establish a unified theoretical framework for optimizing next generation electro-optic, thermo-optic and nonlinear photonic applications by systematically analyzing the optical and thermal characteristics of these systems. Understanding how these external fields, thermal environments, and composition affects these materials is critical for developing advanced quantum electronic devices, like wavelength-tunable infrared modulators, frequency convrters, sensors and thermally stable semiconductor lasers.

CONTENTS

List of Tables

List of Figures

List of Abbreviations and Symbols

Abbreviation	Full Form
AQW	Asymmetric Quantum Well
CDM	Compact Density Matrix
DFT	Density Functional Theory
EMA	Effective-Mass Approximation
FEM	Finite Element Method
FWHM	Full Width at Half Maximum
IR	Infrared
MCE	Magnetocaloric Effect
QCSE	Quantum-Confined Stark Effect
QW	Quantum Well
RCP	Refrigerant Capacity
SHG	Second Harmonic Generation
SOI	Spin-Orbit Interaction
SQW	Step Quantum Well
THG	Third Harmonic Generation
2D	Two-Dimensional

List of Symbols

Symbol	Description	Unit (SI)
α	Linear absorption coefficient	m^{-1}
$\alpha^{(1)}$, $\alpha^{(3)}$	Linear and third-order absorption coefficients	m^{-1}
β	Varshni temperature parameter (430 K)	K
Γ_{ij}	Dephasing rate (intersubband)	s^{-1}
Δn	Refractive index change	dimensionless
ε_0	Vacuum permittivity	$F \cdot m^{-1}$
$\hbar$	Reduced Planck constant	$J \cdot s$
μ_0	Vacuum permeability	$H \cdot m^{-1}$
ω	Angular frequency of light	$rad \cdot s^{-1}$
$\chi^{(2)}$	Second-order susceptibility (SHG)	$m \cdot V^{-1}$
$\chi^{(3)}$	Third-order susceptibility (THG)	$m^2 \cdot V^{-2}$
B	Magnetic field	T
C	Heat capacity (per quantum well)	$eV \cdot K^{-1}$
c	Speed of light in vacuum	$m \cdot s^{-1}$
E	Electric field	$V \cdot m^{-1}$ or $kV \cdot cm^{-1}$
E_g	Bandgap	eV
E_i	Subband energy (i = 1,2,3,4)	eV
F	Helmholtz free energy	eV
I	Optical intensity	$W \cdot m^{-2}$
k_B	Boltzmann constant	$eV \cdot K^{-1}$
L	Well width	m
M_{ij}	Dipole matrix element	$C \cdot m$
m*	Electron effective mass	kg
m_0	Free electron mass	kg

Symbol	Description	Unit (SI)
N_s	Sheet carrier density	m^{-2}
N_v	Volume carrier density	m^{-3}
n_r	Refractive index	dimensionless
P	Hydrostatic pressure	GPa
q	Elementary charge	C
S	Entropy	$eV \cdot K^{-1}$
T	Temperature	K
T_1	Population relaxation time	s
T_2	Dephasing time	s
U	Mean (internal) energy	eV
V(z)	Confining potential	eV
x	Selenium mole fraction in $As_2(Se_xTe_{1-x})_3$	dimensionless
Z	Canonical partition function	dimensionless

CHAPTER 1
LITERATURE REVIEW

1.1 Introduction

Nanomaterials have changed the semiconductor field. Nanomaterial are different from bulk materials becuase unlike bilk materials, they can exhibit energy quantization. Confining elctron in one direction makes its energy discrete. This is the basis of quantum dots, quantum wires and quantum wells [7,65]. They are particularly useful becuase these qunatized energies can be tuned up or down for a particular wavelength. This make nanomaterials perfect candidates for lasers, modulators, detectors, and frequency converters[16,91,95]. But most of the work in last forty years in quantum wells is on III-V materials like GaAs and InP[16,60]. They were the standard for fabricating quantum wells. This study suggests two distinct material alternatives. The first is a ternary chalcogenide alloy, As_2SeTe[66,101]. The second is a two-dimensional transition metal dichalcogenide, MoS_2[58.89].

Some concerns with nanomaterial devices are their tunabilty and thermal stabilty. This work investigates the same. First, the tunability of these material systems in response to the composition of material and external peturbations like E field, B field , pressure and tempuratre. The second being its thermal stability and various resposnes under same conditions.

1.2. Problem Statement and Objectives

In modern times, the need for highly efficient, thermaly stable devices which operatesin mid infra red and terahertz range[16,95,108]. Terahertz source needs strong SHG or THG. Traditional bulk semiconductors does not meet this demand[107,110]. We need greener, safer and cheaper alternatives tostandard materials we already use.

Now there are tons of studies around the tunabilty of these nanomatirals via external perturbatiopns. But most of these studies the behaviour of these nanomaterials in isolated environment with one perturbation at a time[43,59,105]. This does nopt give the best picture of the behavior of the materilas in practical applications.

The objective of this group of studies is is to studythe altrnatives to the toxic materials like GaAs and InP which we use in nanomaterial research and applications[66,101,8]. It aims to investigate the optical and thermal behaviours of two spcific materials, one is $As_2(Se_xTe_{1-x})_3$ and another is MoS_2. The properties are explored in quantum well systems with a broken symmtery using step within the wells. We explore various optical and thermal properties of these material systems to invesatigate there tunabilty using compostion and external purterbations.

Another objective is to understand how these material behaves under various simultaneous purterbations. We applied various perturbations like Electric field, magnetic feild, Hydrostaic pressure and termpurature simultaneous on both materials[18,23,25]. We varied one factor at a time keep all other fixed at a low non zero value. This simulatanoues application of perturbations gives a better tunability and is closer to practical applications.

1.3 Literature review

1.3.1 Chalcogenide-Based Quantum Wells

Chalcogenide glasses have attracted growing interest for nonlinear photonics, mainly because of their wide infrared transparency window and large $\chi^{(3)}$. Mortazavi et al. [66] studied As_2S_3, As_2Se_3, and As_2Te_3 nanosheets and showed them to be superstretchable semiconductors with anisotropic carrier mobilities. Cheng et al. [20] confirmed the large refractive index and high nonlinearity of As_2Te_3 in a study of its bonding and optical properties. Behera and Naik [8] tracked how optical properties evolve in laser-induced Te/As_2Se_3 thin films.

On the waveguide side, Wang and Dai [107] reviewed mid-infrared supercontinuum generation in chalcogenide fibres, while Xiong et al. [110] laid out a broader roadmap for integrated nonlinear photonics with these materials, and Gai et al. [31] characterised GeSbS glass waveguides.

All of these studies, however, deal with bulk or waveguide geometries. No prior work has examined composition-dependent intersubband optical properties in $As_2(Se_xTe_{1-x})_3$ step quantum wells — a gap that directly motivates the present study. The composition-dependent bandgap relation we use derives from Ho [38], who studied the electronic structure of $As_2(Se_xTe_{1-x})_3$ and $As_2(Se_xTe_{1-x})_3$ crystals. Brandová et al. [13] confirmed that the alloy remains amorphous across the full composition range, which is important for the stability of any device fabricated from it. Parchanski et al. [76] measured $\chi^{(3)}$ values of 4.9–7.5 × 10^{-12} esu (roughly 3–5 × 10^{-20} m^2/V^2) in thin films of the related $(As_2Se_3)_{80-x}(As_2Te_3)_x(SnTe)_{20}$ system; these match our calculated values well.

1.3.2 MoS_2-Based Quantum Wells

MoS_2 has been studied intensively since the isolation of its monolayer form. Liu et al. [158] reviewed the role of spin-orbit coupling, electric field, and strain, noting the strong spin-orbit interaction and the direct bandgap at the K point that distinguish monolayer MoS_2 from the bulk. Newaz et al. [67] had demonstrated electrical control of the optical properties in the monolayer, focusing on excitonic transitions in the visible range. But our study is physically distinct since we are concerned with intersubband transitions in the far-infrared and terahertz regime.

The band parameters we use in this material study come from the DFT calculations of Rostami and Asgari [89], who have studied the similar electronic structure of MoS_2 under electric and magnetic fields. Wen et al. [108] investigated the uses of terahertz optical properties tuned by magnetic field, and Dahiya et al. [23] provided us the methodological framework for using distinctive hydrostatic pressure and temperature that we adapt here for our study of MoS_2.

To our knowledge, we can claim that no previous study has reported for the study for intersubband nonlinear optical response for an asymmetric quantum well built entirely from MoS_2 material parameters. And from this work we attempt to closes that gap.

1.3.3 Linear and Nonlinear Absorption

The standard theoretical framework for intersubband absorption in quantum wells was initiated mainly by the works of Ahn and Chuang [2]. On observing the trends, we note that the linear absorption coefficient $\alpha^{(1)}(\omega)$ has a Lorentzian lineshape peaked at $\hbar\omega = E_{21}$, with a linewidth which is controlled by the dephasing time T_2. The third-order property $\alpha^{(3)}(\omega, I)$ was derived in detail by Guo et al. [34]. By which we see that near resonance it is negative, producing saturable absorption, and the total absorption is thus the sum of the linear and third order contributions.

Sari et al. [91] showed that step-well geometries account for the occurrence of nonlinear response relative to square wells. It occurs due to the system's geometry, thus asymmetry generates non-zero diagonal dipole differences, which account for third order effects. Chen et al. [19] added that the electric field dependence for parabolic wells, demonstrates that both of the peak position and peak magnitude vary continuously due to field strength.

1.3.4 Second Harmonic Generation

Second harmonic generation (SHG) needs broken inversion symmetry to occur. In a perfectly symmetric well the triple product $M_{12}\cdot M_{23}\cdot M_{31}$ vanishes due to symmetry, therefore $\chi^{(2)} = 0$. The idea of using asymmetric quantum wells as synthetic nonlinear materials goes back to Gurnick and DeTemple [36].

Fejer et al. [30] measured quadratic susceptibilities of order 10^{-10} m/V in electric-field-biased AlGaAs wells such that the values that match our own calculations for Te-rich $As_2(Se_xTe_{1-x})_3$ compositions and that provides an important validation of the theoretical approach. Kasapoglu et al. [43] examined SHG and optical rectification in asymmetrical semi exponential wells under external fields and found that an applied electric field shifts and enhances the SHG peaks. Ortolani et al. [73] have reported $\chi^{(2)}$ values as large as 10^{-8} m/V in Ge/SiGe asymmetric wells operating under the condition of double resonance, which suggests that further structural optimisation of our wells can lead to further additional gains.

1.3.5 Third Harmonic Generation

Third harmonic generation (THG) is a $\chi^{(3)}$ process: three photons at ω combine to produce one at 3ω. Unlike SHG, it does not require a non-centrosymmetric structure, though asymmetry still enhances it in practice.

Lu et al. [59] calculated $\chi^{(3)}$ values in the range 10^{-20}–10^{-18} m^2/V^2 for GaAs/GaAlAs exponentially confined wells with electric and magnetic fields applied. Ungan et al. [106] showed that the peaks of THG narrow and sharpen under strong confinement in semi parabolic wells. Dakhlaoui [25], in the asymmetric triple well study has been already mentioned, found that pressure suppresses THG by more than 95% over 0–3 GPa. This result closely parallels with what we found for MoS_2 asymmetric wells.

1.3.6 Partition Function Formalism

The thermodynamic behaviour of a quantum confined system is mostly described within the canonical ensemble. The partition function $Z = \Sigma \exp(-Ei/kBT)$ is the main equation from which we calculate all the thermodynamic properties that we have to study.

Boyacioglu and Chatterjee [11] studied heat capacity and entropy in a GaAs quantum dot with Gaussian confinement and identified a characteristic Schottky anomaly in the specific heat. A peak that appears when k_{BT} is comparable to the energy gap between the ground state and the first excited state. Khordad and Rastegar Sedehi [50] found that with temperature in one-dimensional quantum wires under Rashba spin orbit interaction and magnetic field, with saturation at high T it constitutes for the increasing entropy. And Servatkhal et al. [93] compared Shannon and Tsallis formalism for three-dimensional quantum wires and found qualitative agreement between the two approaches.

1.3.7 Heat Capacity and the Schottky Anomaly

The Schottky anomaly directly influences the discrete energy levels. At low temperature, essentially all carriers sit in the ground state and the heat capacity is small. As thermal energy grows to match the level spacing, C_v rises sharp and then falls back as higher levels become populated uniformly. Khordad and Mirhosseini [49] reproduced this peak quantitatively for GaAs quantum dots with effective-parabolic confinement and showed that the peak position tracks the confining potential strength. Later Khordad and Rastegar Sedehi [51] have found that changing the ring radius in double ring-shaped dots broadens and shifts the peak. Further Gupta et al. [35] demonstrated that both electric and magnetic fields move the peak in conical quantum dots, an effect further confirmed by Castaño-Yepes et al. [17] for two-dimensional dots with topological defects and Rashba coupling.

1.3.8 Magnetocaloric Effect

The magnetocaloric effect (MCE) measure entropy changes when we apply a magnetic field isothermally, which is given as : $\Delta S = S(B,T) - S(0,T)$, whereA negative ΔS means the field reduces disorder; a positive value means it increases it.

Rastegar Sedehi and Khordad [86] further showed that ΔS can actually change sign as a function of temperature in tuned quantum dot/ring systems — a crossover from conventional to inverse MCE that is a distinctive signature of quantum confinement. Rastegar Sedehi [85] also found that the both field strength and spin-orbit coupling independently tunes the MCE magnitude in narrow nanowire quantum dots. Priyanka et al. [78] reported that impurities suppress the MCE but leave the crossover temperature largely unaffected in GaAlAs quantum wires. Olendski [72] noted that entropy in one-dimensional quantum wells is remarkably insensitive to electric field, because the Stark shift displaces all levels roughly rigidly without changing their spacings.

1.3.9 Research Gap and Present Contribution

A review of the literature points can lead to several clear gaps.

Most chalcogenide work concerns bulk or waveguide geometries; composition-dependent intersubband studies of $As_2(Se_xTe_{1-x})_3$ step wells do not exist. Previous nonlinear optical studies of quantum wells have examined at most two external perturbations simultaneously; no study has applied temperature, electric field, magnetic field, and hydrostatic pressure together within a single framework. MoS_2 quantum well studies have concentrated on excitonic transitions in the visible range, leaving the far-infrared and terahertz intersubband regime essentially unexplored.

Thermodynamic properties of step quantum wells in chalcogenide alloys have not been reported; the existing literature focuses on simple square or parabolic GaAs wells. Finally, combining nonlinear optical and thermodynamic analysis on the same material system is uncommon — most publications address one or the other.

This work addresses all five gaps. For the chalcogenide system, we present the first systematic study of composition-dependent intersubband optical properties and demonstrate three-parameter tunability — through composition, electric field, and magnetic field — that provides continuous mid-infrared spectral coverage. For MoS_2, we report the first theoretical prediction of intersubband nonlinear optical response in an asymmetric quantum well and apply all four perturbations simultaneously, showing that each produces distinct and sometimes opposing trends. For both systems we compute the full set of thermodynamic quantities — mean energy, Helmholtz free energy, entropy, heat capacity, and the magnetocaloric effect — and trace how composition and each external perturbation tunes them.

CHAPTER 2

THEORETICAL FRAMEWORK AND METHODOLOGY

2.1. Effective Mass Approximation

The electronic states of a carrier confined within a semiconductor heterostructure are governed by the many-body Hamiltonian equation of the crystal which encompasses the periodic ionic lattice potential, electron to electron interactions, and all relevant perturbation terms. A direct solution of this problem is computationally intractable for any device-relevant geometry. The effective mass approximation (EMA) provides us with a rigorous and well-validated simplification for the system [7]. Instead of tracking how an electron bumps into a repeating grid of atoms, we simplify everything by giving the electron a new, adjusted mass called the effective mass. The entire crystal structure depends on this adjusted mass, thus we can apply the same mechanism to an electron in free space.

Solving the full Schrödinger equation for a semiconductor heterostructure is impossible. You have millions of atoms. Each has its own potential. But we do not need all that detail. Near the band edge, the electron behaves like a free particle. But it does not have the free electron mass. It has an effective mass.The effective mass comes from the band structure [7,65]. In a periodic crystal, the electron feels the lattice potential. That potential curves the energy bands. Near the bottom of the conduction band, the energy-momentum relation is approximately parabolic:

$$E(k) \approx E_g + \frac{\hbar^2 k^2}{2m} \tag{2.1}$$

where the effective mass is defined through the inverse curvature of the dispersion surface,

$$\frac{1}{m*} = \frac{1}{\hbar^2} \cdot d^2E(k)/dk^2 \ \{k=0\}. \tag{2.2}$$

Here, m* is not the free electron mass m_0. It is smaller or larger depending on the material. For MoS_2,
m* ≈ $0.47m_0$ [89,74]. For As_2Te_3, it is even lighter. For As_2Se_3, it is heavier. This parabolic approximation is used for the lowest conduction-band states at moderate wavevectors, which are precisely the states relevant to intersubband transitions in the far-infrared to terahertz range considered here. In a heterostructure, spatial variation of the composition across interfaces produces a position-dependent effective mass m*(z) and a piecewise potential profile V(z). The appropriate single-band envelope-function equation is the BenDaniel–Duke Hamiltonian, which is given by [65]:

$$\frac{-\hbar^2}{2}\frac{d}{dz}\left(\frac{1}{m^*(z)}\frac{d\psi(z)}{dz}\right) + V(z)\psi(z) = E\psi(z) \tag{2.3}$$

In a quantum well, the electron is free in the xy plane of the well but confined along z. The in-plane motion contributes a kinetic energy $\hbar^2k\|^2/(2m^*)$, and the total energy separates into in-

plane and confinement parts. The confinememnt energy is what is only important for intersubband transitions. That is what we compute. The approximation is valid when the envelope function varies slowly compared to the lattice constant. For the structures studied here, well widths are 4–20 nm, well above the ~0.3 nm lattice scale. It also requires that the relevant electron states sit near the minimum band, which is satisfied for the low-lying conduction band states.

Although for the chalcogenide system, there is one complication. $As_2(Se_xTe_{1-x})_3$ is amorphous. It lacks long-range crystalline order [101,13]. Strictly, Bloch's theorem does not apply here. But the short-range order in amorphous chalcogenides is well preserved. The local bonding geometry is nearly the same as in the crystalline phase. The envelope function approximation remains valid as long as the region trapping the electron is larger than the microscopic area affected by defects or imperfections in the crystal. For the wells studied here, quantum confinement energies of 190–600 meV are far larger than the band-tail extent of 50–100 meV [77]. The electrons occupy extended-like states, not tail states. The EMA framework is justified and has been applied to amorphous heterostructures in the literature. In case of MoS_2, It is crystalline. The effective mass is well defined from experimental data and DFT calculations. We use $m*=0.47m0$ at room temperature and zero pressure. But it changes with temperature (Varshni) and pressure (Kane model). Those dependencies are discussed further.Thus, the effective mass (m*) in each alloy region depends on composition through the k·p Kane relation [12],

$$\frac{m_0}{m^*(x)} \approx 1 + \frac{E_P}{E_g(x)} \tag{2.4}$$

where E_P is the Kane energy and $E_g(x)$ is the composition-dependent bandgap. It is one of the primary physical levers in the composition-dependent results of Chapter 3.

where m_0 is the free-electron mass, E_P is the Kane energy, and $E_g(x)$ is the local alloy bandgap. As the Se fraction x increases in the chalcogenide alloy, the bandgap widens [38]. A wider bandgap gives a heavier effective mass. This directly affects the subband spacing and the dipole matrix elements. Equation (2.2) captures the essential inverse relationship between bandgap and effective mass that underlies the composition-dependent and temperature- and pressure-dependent results. Perturbation dependent modifications of E_g through the Varshni relation (temperature) and the deformation potential (pressure), are used directly into m* through Eq. (2.2) and are incorporated self-consistently in the COMSOL finite element model [74].

2.2. Perturbations

The single-electron Hamiltonian for a quantum well under applied external perturbations contains four contributors mainly, the confining potential that defines the heterostructure, a linear term from an applied electric field, a quadratic term from a perpendicular magnetic field, and modifications to the bandgap and effective mass due to hydrostatic pressure and temperature. All these are used for our study in the quantum well based hamiltonian used

throughout this work. Thus, The one-dimensional time-independent Schrödinger equation is written as:

$$\frac{-\hbar^2}{2}\frac{d}{dz}\left(\frac{1}{m^*(z)}\frac{d\psi(z)}{dz}\right) + V(z)\psi(z) = E\psi(z) \quad (2.5)$$

where $\hbar$ is the reduced Planck constant, m*(x,T,P) is the position,temperature as well as pressure-dependent effective mass used throughout our study, $\psi(x)$ is the envelope wavefunction, and E is their corresponding energy eigenvalue. The total potential V_{tot} (x) combines this study of the built-in confinement with the applied external field contributions.

2.2.1 Confining Potential (Step Well / Asymmetric Well)

The confinement potential is the foundation of the whole problem since it defines the our well. The energy levels, the wavefunctions, the optical matrix elements and everything else follows from it. Two different confinement profiles are used in this thesis. For the $As_2(Se_xTe_{1-x})_3$ system, a step quantum well is designed. For MoS_2, an asymmetric quantum well is constructed. The confinement potential $V_0(z)$ defines the heterostructure geometry and constitutes the zero order term in the total Hamiltonian. In this work, a step quantum well system is used for both material systems, MoS_2 and $As_2(Se_xTe_{1-x})_3$ in which two well regions of different potential depths are laterally put between two barrier layers. This geometry breaks spatial inversion symmetry along the growth direction which as we know is a necessary condition for existence of the second-order nonlinear optical susceptibilities [36, 91].

For the chalcogenide system, the confinement depths and effective masses in each region are determined by the local alloy composition x through the composition-dependent bandgap $E_g(x)$ and the associated band offset fractions. The step-well geometry is constant across all composition values, but the potential depths and the position-dependent effective masses are varied continuously with x, making the potential profile itself a tunable parameter of the system. The potential consists of four regions along the growth direction. A left barrier, a shallow well, a deep well, and a right barrier. The conduction band offsets determine the depth of the potential well, which varies with local composition [38,56]. Thus potential is defined as:

$$V(z) = \begin{cases} (V_{barrier} + qF_z) + \frac{1}{2m_{bar}}\ ((\hbar k_y) + (qB_x z))^2 \text{ for z in barrier regions} \\ (V_{step} + qF_z) + \frac{1}{2m_{sh}}\ ((\hbar k_y) + (qB_x z))^2 \text{ for z in the shallow well} \\ (V_{dp} + qF_z) + \frac{1}{2m_{dp}}\ ((\hbar k_y) + (qB_x z))^2 \text{ for z in the deep well} \end{cases} \quad (2.6)$$

where the values used in the paper are $V_{barrier}$=0.6 eV, V_{step}=0.19 eV, and V_{dp}=0.0 eV whereasthe widths are L_{b1}=20 nm, L_{w1}=7 nm, and L_{w2}=10 nm.

Asymmetric quantum well (MoS_2): The geometry follows the parameters from the asymmetric quantum well model [23,18]. Here we define four intervals. The left barrier (0–8 nm, 300 meV), the primary well (8–12 nm, 0 meV), the secondary well (12–20.5 nm, 80 meV), and the right

barrier (20.5–28.5 nm, 300 meV). For the MoS_2 system, the potential is defined piecewise along the growth direction x as:

$$V_0(x)=\begin{cases}300\text{ meV} & x< 8\text{ nm}\\ 0\text{ meV} & 8 \le x< 12\text{ nm}\\ 80\text{ meV} & 12 \le x< 20.5\text{ nm}\\ 300\text{ meV} & 20.5 \ge 28.5\text{ nm}\end{cases} \quad (2.7)$$

The total domain is 28.5 nm. The primary well is 4 nm wide and sits at zero potential. The step region is 8.5 nm wide and sits 80 meV above the primary well. Both are enclosed by 300 meV barriers of width 8 nm.

The structure becomes optically useful specifically due to the asymmetry between the two wells. The wavefunctions localise differently in the two regions. The ground state exists in the primary well. The first excited state spreads across both. The difference in localisation is what gives non zero values to the off-diagonal matrix elements M_{12}, M_{23}, and M_{31}. These are the quantities that determine the strength values of absorption, SHG, and THG. A symmetric well should have $M_{22} = M_{11}$ and the triple product $M_{12}M_{23}M_{31}$ would vanish identically [36,94]. The step geometry breaks this. It keeps the triple product finite and tunable. Thus no second harmonic terms exist.

2.2.2 Electric Field Term

The electric field term applied to the hamiltonian in our quantum well study is studied here. The application of a static electric field E_x along the heterostructure growth axis introduces a linear perturbation to the total potential energy. An electric field applied along the growth direction adds a linear potential to the Hamiltonian. This is the quantum-confined Stark effect [61,62]. The term ius given by:

$$V_E(x) = q \cdot E_x \cdot x \quad (2.8)$$

where q denotes the electron charge. This term is added to $V_0(x)$ in each spatial interval part of the material based well geometry, producing a spatially tilted total band profile. The resulting changesin the subband energies and wavefunctions constitutes the Quantum-Confined Stark Effect (QCSE).

The physical picture is that one end of the well is raised in energy relative to the other. The electron in the ground state, sitting in the narrow primary well, feels this slope and shifts slightly toward the lower end. The excited states, being more spread out, also shift but by different amounts. The gap between the ground state and the first excited state narrows. The absorption resonance moves to lower photon energies — a redshift.

The ground-state wavefunction and the excited-state wavefunction are shifted in slightly different directions and thus their spatial overlap decreases [61,111]. The transition matrix element M_{12} gets smaller. The absorption peak not only shifts but also weakens.The electric

field perturbations in the MoS_2 study covers the values E_x = 0, 8, 16, and 24 kV/cm, with all other perturbations are kept at their base values. The highest value of the electric field applied of 24 kV/cm is imposed by the condition that the ground-state energy E_1 must remain positive. Numerical calculations shows that E_1 approaches zero near 26 kV/cm, beyond which the electron is no longer bound within the well and the effective-mass framework loses validity. The linear tilt is added directly to the confinement potential in each interval of the geometry. The ground state, which is tightly localised in the narrow primary well, responds more strongly to this tilt than the delocalized excited states. So E_1 drops faster than E_2 and thus the transition energy E_{21} decreases. Consequently, the absorption peak redshifts and this is known as the Quantum-Confined Stark Effect(QCSE) [61], discussed in detail in Section 1.4.1.The field is incorporated into the COMSOL model as a spatially continuous additive term applied uniformly across all four intervals of the domain, consistent with the assumption of a spatially uniform applied field.

2.2.3 Magnetic Field Term

The magnetic field term which is applied perpendicular to the growth direction (along *x*) is used via the vector potential A. An in-plane magnetic field $B_x$that is directed towards the x-axis is incorporated through the minimal coupling substitution [14,105] $p_y \rightarrow p_y + qA_y$, with the Landau gauge vector potential A = (0, B_x · z, 0). Choosing the Landau gauge A=(0,Bxx,0) makes the kinetic momentum as p+*e*A. The resulting contribution to the Hamiltonian is expanding the kinetic energy operator $(p + qA)^2/(2m^*)$ and retaining the leading contribution for $k_y = 0$ which gives the diamagnetic potential energy term. The resulting contribution to the Hamiltonian is:

$$V_B(x)=2m^*(x,T,P)e^2B_x^2x^2 \qquad (2.9)$$

This is a parabolic confining term in z direction [105]. It adds to the existing potential and pushes the wavefunctions toward the centre of the well. It further adds harmonic confinement on top of the existing step-well profile. The total confining potential becomes stiffer as B increases. All subband energies shift upward. Higher subbands shift more because their wavefunctions sample larger values of z^2 [14,104]. The transition energy E_{21} increases. The resonance blueshifts.

In the COMSOL model, this term appears explicitly in the potential energy expression for each interval. The same parabolic term is present in all four regions — barriers, primary well, and step well. The magnetic field is swept from 0 to 12 T. Above roughly 25 T, Landau level phenomenon begins to dominate and the effective-mass picture becomes less reliable. An additional term $2m^*\hbar^2k_y^2$ arises from the in-plane kinetic energy. It is a constant shift and does not affect intersubband differences. In this study, k_y is further set to zero for simplicity.

2.2.4 Pressure-Dependent Bandgap and Barrier Heights

Hydrostatic pressure acts on the crystal lattice by compressing interatomic distances. This raises the bandgap.The bandgap increases linearly with pressure through the deformation potential [68]:

$$E_g(P) = E_{g_0} + a_{pressure} \cdot P \tag{2.10}$$

where $a_{pressure}$ = 12 meV/GPa for MoS_2. The barrier height also changes with pressure. The pressure coefficient for the barrier is dV/dP = 50 meV/GPa. For the step region, the coefficient is scaled proportionally such that $dV_{step}/dP = dV/dP \times V_{step}/V_{barrier}$. The barrier heights scale proportionally to the bandgap. With dV/dP=50 meV/GPa for MoS_2 barriers [23]. For the step potential (80 meV), a smaller coefficient dV/dPstep=2.136×10−30 m^3 is used. Pressure is varied from 0 to 3 GPa across the material system. So under pressure, three things happen simultaneously. The bandgap increases. The barrier height increases. And due to the Kane relation, the effective mass also increases. The wavefunctions become more localised within their respective sub-well regions. The transition energy E_{21} rises steeply. The resonance blueshifts at a rate of about 6 meV/GPa in MoS_2 — the largest spectral shift rate of all four perturbations. The localisations works against the nonlinear response. As the linear absorption doubles, the nonlinear susceptibilities can drop by 90% or more across the material system. The pressure sweep runs from 0 to 3 GPa in this work. Above roughly 15 GPa is where the phase transition in MoS_2 begins [68].

2.2.5 Temperature-Dependent Bandgap (Varshni) and Effective Mass (Kane)

Temperature affects the bandgap through electron-phonon interactions. Temperature enters through the bandgap. As temperature rises, the crystal lattice expands and the electron–phonon interaction strengthens. Both effects reduce the bandgap. The Varshni relation provides an empirical fit [15,16]:

$$E_g(T) = E_g(0) - \frac{\alpha T^2}{T+\beta} \tag{2.11}$$

where E_g(0) = 1.9 eV for MoS_2, α = 0.54 meV/K, and β = 430 K. At *T*=200 K, the bandgap reduction is about 34 meV. At 500 K, the bandgap reduction is rather larger. The bandgap reduction is used directly into the effective mass equation through the Kane relation. A smaller E_g gives a lighter effective mass m* whereas a lighter electron is less tightly confined [74]. Its wavefunction spreads slightly outward from its equilibrium region. In an asymmetric well, the ground state loosens more than the excited states because it starts from a steeper spatial gradient. The gap E_{21} increases slightly and the resonance nudges upward. The blueshift from temperature is less than 1 meV across the full 200–500 K sweep. It is the weakest perturbation in this study by a considerable margin. In the COMSOL model, the effective mass uses both temperature and pressure effects in a single expression,

$$m_{eff}(T, P) = m_{eff0} \times [E_{g0} + a_{pressure} \cdot P - \alpha \cdot T^2/(T+\beta)] / E_{g0}. \quad (2.12)$$

This expression is evaluated at each point in the mesh and for every parameter combination. It ensures that the two bandgap mechanisms, one raising E_g, the other lowering it and is treated consistently and simultaneously.

2.3 Finite Element Method Implementation

The Hamiltonian containing the Schrödinger equation with cannot be solved analytically for step or asymmetric wells. Thus we use the potential as a piecewise function where the effective mass changes abruptly at interfaces and external fields are added on the account of position dependent terms. Due to this, we use the numerical method. This study uses the finite element method (FEM) as implemented in COMSOL Multiphysics[22,26,97]. Here we use the Semiconductor Module which provides us a dedicated Schrödinger Equation interface for solving such eigenvalue problems.

In the FEM method, the domains are divided into tiny fragments. Within each element, the wavefunction is approximated by using simple polynomial functions. The differential equation is then converted into a matrix eigenvalue problem. The solution converges as the mesh is refined. Quadratic Lagrange elements are used here because they give better accuracy for second-order derivatives like the kinetic energy term [22, 97].

2.3.1 Geometry and Mesh

The computational domain spans the entire quantum well structure. For MoS_2, the total length is 28.5 nm. We define the four intervals as left barrier (0 to 8 nm), primary well (8 to 12 nm), secondary well (12 to 20.5 nm), and right barrier (20.5 to 28.5 nm). In case of, $As_2(Se_xTe_{1-x})_3$, the geometry is similar but we use different widths, left and right barriers of 20 nm, shallow well of 7 nm, and deep well of 10 nm, giving a total length of 57 nm. The Schrödinger equation with a piecewise potential and a position-dependent effective mass does not have a closed-form analytical solution for the step-well geometry used here [7,65]. Thus to compensate this loss, finite element method (FEM) is used throughout this work, implemented in COMSOL Multiphysics.

The domain is meshed using quadratic Lagrange elements. The mesh contains 1002 edge elements[22], giving 1003 vertices across the 28.5 nm domain. This works out for roughly one mesh point every 0.028 nm well below the scale of any wavefunction variation condition. This number is chosen after a convergence test: increasing the element count further changes the eigenvalues by less than 0.01 meV. The mesh is uniform across the domain and is therefore sufficiently fine for the precision needed in the optical property calculations.Quadratic elements are used rather than linear ones because the second spatial derivative in the Schrödinger equation requires at least quadratic basis functions to represent accurately [22]. With linear

elements, the curvature of the wavefunction would be approximated as piecewise constant, which is too crude for eigenvalue problems.

The four intervals in COMSOL are defined as follows. Interval 1 runs from 0 to 8 nm and carries the left barrier potential of 300 meV. Interval 2 runs from 8 to 12 nm and is the primary well at zero potential. Interval 3 runs from 12 to 20.5 nm and is the step well at 80 meV. Interval 4 runs from 20.5 to 28.5 nm and carries the right barrier at 300 meV. The perturbation terms electric field, magnetic field, pressure, temperature are added as additional expressions within each interval respectively.

2.3.2 Boundary Conditions

We impose Dirichlet boundary conditions at the left and right ends of the domain [7,22]. That means the wavefunction is set to zero given by: $\psi(0)=0,\psi(L)=0$. This simulates infinite barriers. It is a standard approximation for quantum wells where the actual barrier heights are large (300 meV or more) compared to the confined state energies (tens to a few hundred meV). The condition forces the wavefunction to vanish at the boundaries, which is physically correct for a particle trapped in a box with impenetrable walls.

No additional boundary conditions are needed at internal interfaces. The finite element formulation naturally enforces continuity of the wavefunction and conservation of probability current in the equation. The position dependent effective mass inside the derivative is handled automatically. At $x = 8$ nm, 12 nm, and 20.5 nm no additional boundary conditions are imposed directly. COMSOL handles the heterojunction continuity conditions automatically through the BenDaniel Duke operator form of the kinetic energy. The continuity of ψ and of $(1/m^*)(d\psi/dz)$ across each interface is enforced weakly through the finite element assembly[65]. It is the condition that preserves probability current across a heterojunction with a position-dependent effective mass.

2.3.3 Eigenvalue Solver Settings

The eigenvalue study is configured to find the lowest bound states. We request 20 eigenvalues for each simulation. The search is centered around 0.1 eV (100 meV) because the intersubband transitions of interest lie in the mid-infrared to terahertz range (roughly 8–140 meV). The eigenvalue scale is set to 1 eV to improve numerical conditioning. The FEM discretisation converts the Schrödinger equation into a matrix eigenvalue problem of the form

$$K \cdot u = \lambda \cdot M \cdot u, \qquad (2.13)$$

where K is the stiffness matrix assembled from the kinetic and potential energy operators, M is the mass matrix from the FEM basis functions, u is the vector of nodal wavefunction amplitudes and λ contains the energy eigenvalue values.

The solver uses an iterative algorithm (ARPACK) designed for large sparse matrices. The tolerance for convergence of eigenvalue is set to $1\times10-10$. The parameter sweeps are implemented just like the nested loops in the COMSOL parametric solver. For each combination of x, T, B, E_x, and P, a fresh eigenvalue solve is performed. The resulting eigenvalues and integrated dipole matrix elements are exported to MATLAB for post-processing. The MATLAB code then computes all optical and thermodynamic properties from these inputs.

2.4 Density-Matrix Formalism

Once we are done calcuating the energy eigenvalues and use them to further calculate the dipole matrix elements, the optical properties of the quantum well can be calculated from there on. We use the density-matrix formalism approach to get these properties. It describes how the electron population distributes among subbands when light shines on the material structure. The incident electromagnetic field couples to the electron through the dipole interaction. The result is a set of expressions for the linear and nonlinear susceptibilities.

We work within the compact density-matrix approach, which assumes a two-level approximation for absorption and refractive index changes. For harmonic generation, three-level or four-level models are used because they involve multiple intermediate states. The broadening of the transitions is included through taking the dephasing rate as $\Gamma_{ij}=1/T_2$, where T_2 is the dephasing time. In this work, we take $T_2=150$ fs specifically, which gives $\hbar\Gamma_{21}\approx4.4$ meV. The carrier density is taken as the volume density $N_v=N_s/L_w$, where $N_s=5\times1015$ m^{-2} and L_w is the total well width (28.5 nm for MoS_2, 57 nm for $As_2(Se_xTe_{1-x})_3$). All formulas below are written in SI units. The dipole matrix element between subbands i and j is defined as $M_{ij} = \langle\psi_i|ez|\psi_j\rangle$, with e the elementary charge. The transition energy is $E_{ij}=E_j-E_i$.

2.4.1 Linear and Third-Order Absorption Coefficients

The linear absorption coefficient $\alpha^{(1)}(\omega)$ describes how much light is absorbed at low intensity. It is derived from the first-order susceptibility. The linear absorption coefficient $\alpha^{(1)}(\omega)$ arises from the single-photon transition between the ground state and the first excited state. For a transition from the ground state (1) to the first excited state (2), the expression is:

$$\alpha^{(1)}(\omega) = \frac{\omega\mu_0 c}{n_r}\sum_{i<j}\frac{|M_{ij}|^2 (n_i-n_j)\hbar\Gamma_{ij}}{(E_j-E_i-\hbar\omega)^2+(\hbar\Gamma_{ij})^2} \qquad (2.14)$$

Here, ω is the angular frequency of the incident light, n_r is the refractive index, c is the speed of light in vacuum, and ε_0 is the vacuum permittivity. The shape is Lorentzian, peaked at $\hbar\omega=E_{21}$ [2]. The width is determined by Γ_{21}.

At high optical intensities, the third-order nonlinear absorption becomes important. It is negative near resonance, meaning it reduces the total absorption (saturable absorption). The expression for $\alpha^{(3)}(\omega,I)$ is more complicated because it involves the diagonal matrix elements M_{11} and M_{22}:

$$\alpha^{(3)}(\omega, I) = -\frac{\omega\mu_0 c}{n_r}\frac{I}{2\epsilon_0 n_r c}\sum_{i<j}\frac{4|M_{ij}|^4 (n_i - n_j)\hbar\Gamma_{ij}}{\hbar^4\left[(E_j - E_i - \hbar\omega)^2 + (\hbar\Gamma_{ij})^2\right]^2} \quad (2.15)$$

where $\Delta M = M_{22} - M_{11}$. The total absorption is then the sum of linear and third-order contributions:

$$\alpha_{total}(\omega, I) = \alpha^{(1)}(\omega) + \alpha^{(3)}(\omega, I) \quad (2.16)$$

These formulas follow the work of Ahn and Chuang for the linear term and Guo et al. for the nonlinear term [2,34].

2.4.2 Linear and Third-Order Refractive Index Change

The refractive index change Δn is used to show how a phase of light is altered by the quantum well. It is important for the use of modulators and switches. The refractive index change Δn arises from the real part of the susceptibility [2,19]. Similar to the absorption profile, the refractive index change is decomposed into linear and third order contributions. The linear part $\Delta n^{(1)}$ comes from the real part of the first-order susceptibility is written as:

$$\frac{\Delta n^{(1)}(\omega)}{n_r} = \frac{1}{2\epsilon_0 n_r^2}\sum_{i<j}\frac{|M_{ij}|^2 (n_i - n_j)(E_j - E_i - \hbar\omega)}{(E_j - E_i - \hbar\omega)^2 + (\hbar\Gamma_{ij})^2} \quad (2.17)$$

the numerator having $(E_{21} - \hbar\omega)$ affects the property since below resonance, this is positive. Whereas above resonance, it is negative. So $\Delta n^{(1)}$ changes sign at the transition energy. That is the normal dispersion crossing into anomalous dispersion.

The third-order refractive index change $\Delta n^{(3)}$ is more complicated. It depends on I and on the diagonal dipole difference. The full expression is given as:

$$\frac{\Delta n^{(3)}(\omega, I)}{n_r} = -\frac{\mu_o c I}{4\epsilon_0 n_r^3}\sum_{i<j}\frac{|M_{ij}|^2 (n_i - n_j)(E_j - E_i - \hbar\omega)}{\left[(E_j - E_i - \hbar\omega)^2 + (\hbar\Gamma_{ij})^2\right]^2} \times \left[4|M_{ij}|^2 - \frac{(M_{ii} - M_{jj})^2 (3(E_j - E_i)^2 - 4(E_j - E_i)\hbar\omega + \hbar^2(\omega^2 - \Gamma_{ij}^2)}{(E_j - E_i)^2 + (\hbar\Gamma_{ij})^2}\right] \quad (2.18)$$

Thus using both first order and third order refractive index change we get the total refractive index change as:

$$\frac{\Delta n_{total}(\omega, I)}{n_r} = \frac{\Delta n^{(1)}(\omega)}{n_r} + \frac{\Delta n^{(3)}(\omega, I)}{n_r} \quad (2.19)$$

In practice, $\Delta n^{(3)}$ is usually negative near resonance. It lowers the peak of $\Delta n^{(1)}$ and slightly shifts the zero-crossing.The linear refractive index change $\Delta n^{(1)}$ is proportional to the real part of the first order susceptibility, while the third order change $\Delta n^{(3)}$ describes the optical Kerr effect [34,106]. These parameters characterize the phase modulation capabilities of our $As_2(Se_xTe_{1-x})_3$ and MoS_2 quantum well systems, which prove to be useful in applications of optical switching and frequency conversion.

2.4.2 Second Harmonic Generation ($\chi^{(2)}$)

Second harmonic generation is described as the characteristic second order nonlinear process. In this process, two photons of ω frequency combine to produce one photon at 2ω frequency. This process is forbidden in symmetric structures and centrosymmetric systems [36,94].For non-centrosymmetric systems, such as the asymmetric quantum wells investigated in this work, second harmonic generation (SHG) is a dominant nonlinear process [43,30]. The second-order susceptibility $\chi^{(2)}$ depends on products of three dipole matrix elements: M_{12},M_{23} and M_{31}. In a symmetric well, since the wavefunctions have definite parity, the product vanishes. . In our asymmetric step well, we use a three-level model. Therefore, the dominant term in $\chi^{(2)}$ for SHG is:

$$\chi^{(2)}(2\omega) = \frac{Ne^3}{\epsilon_0\hbar^2}\frac{M_{12}M_{23}M_{31}}{(\omega-\omega_{21}+\Gamma_{21})(2\omega-\omega_{31}+i\Gamma_{31})} \quad (2.20)$$

Here, M_{ij} represent the dipole matrix elements, and ω_{ij} are the intersubband transition frequencies. Here, $E_{31} = E_3 - E_1$. The first denominator gives a resonance when $\hbar\omega = E_{21}$. This is callled a one photon resonance. The second denominator gives a resonance when $2\hbar\omega = E_{31}$. That is a two photon resonance. Both peaks appear in the spectrum. The magnitude of $\chi^{(2)}$ is proportional to the product of the three dipoles whose product is sensitive to asymmetry. Thus the more asymmetric the well, the larger $\chi^{(2)}$ can become.

2.4.2 Third Harmonic Generation ($\chi^{(3)}$)

Third harmonic generation is a third-order process. Three photons at frequency ω combine to produce one photon at 3ω [94,106]. Third harmonic generation is different from second order one since it does not require asymmetry but using asymmetrical systems definitely enhances it. The expression for $\chi^{(3)}$ involves four dipole matrix elements and three energy denominators.Using a four-level model, the third order susceptibility is given by:

$$\chi^{(3)}(3\omega) = \frac{N}{\epsilon_0\hbar^3}\frac{Ne^4M_{12}M_{23}M_{34}M_{41}}{\epsilon_0\hbar^3(\omega-\omega_{21}+i\Gamma_{21})(2\omega-\omega_{31}+i\Gamma_{31})(3\omega-\omega_{41}+i\Gamma_{41})} \quad (2.21)$$

where $\omega_{j1} = E_{j1}/\hbar$. The observed resonances occur at $\hbar\omega = E_{21}$ for one photon and $2\hbar\omega = E_{31}$ for two photon and $3\hbar\omega = E_{41}$ for three photons. The product of four dipoles M_{12} M_{23} M_{34} M_{41} is given by the four-level cascade. Unlike SHG, in a symmetric well this product is not zero, but in an asymmetric well it can be larger because the wavefunctions are not orthogonal across different regions [59].

2.5 Canonical Partition Function

The thermodynamic state of the quantum well systems is described using the canonical ensemble, where the system is in thermal equilibrium with a heat reservoir at temperature T. The energy eigenvalues obtained from the Schrödinger equation define a discrete quantum system. For fixed values of external perturbations (electric field, magnetic field, pressure, temperature), the thermodynamic behaviour of this system is described by the canonical

ensemble. The fundamental starting point for getting these thermodynamic properties is the construction of the canonical partition function Z [11, 49, 35], which captures the statistical distribution of the electronic states. Given the discrete nature of the bound states calculated via the Finite Element Method, the partition function is defined as:

$$Z = \sum_{n}^{N} \exp\left(-\frac{E_n}{k_{BT}}\right) \tag{2.22}$$

where E_i are the eigenenergies in joules (or eV) , $k_B = 8.6173\times10^{-5}$ eV/K is the Boltzmann constant, and T is the absolute temperature. The ground state energy E_1 is set as the reference when needed, but the absolute energies matter because they shift with external fields.This summation accounts for the influence of external perturbations such as hydrostatic pressure, electric, and magnetic fields. From Z we derive all thermodynamic potentials. The following relations are standard in statistical mechanics.

2.5.1 Mean Energy

The mean energy U(T), or the internal energy of the electronic system, represents the ensemble average of the energy states. It is derived directly from the partition function by evaluating the logarithmic derivative with respect to the partition function:

$$U = -\frac{\partial \ln Q}{\partial \beta} \tag{2.23}$$

This value provides insight into the energy storage capacity of the quantum well. On applying several field perturbations, the shifts in the subband energies E_i leads to a redistribution of the carrier population, directly altering the internal energy of the system as a function of the external fields. At low temperatures ($k_{BT} \ll E_2 - E_1$), only the ground state contributes and $U \approx E_1$ [11, 50]. At high temperatures, all four states are nearly equally occupied, and U approaches the average of the four energies. The temperature dependence of U shows us how well the thermal energy is absorbed by the electronic subsystem.

2.5.2 Helmholtz Free Energy

The Helmholtz free energy F is a central thermodynamic potential that determines the stability of the system at constant temperature and volume. It relates the internal energy to the entropic contributions of the system. The Helmholtz free energy F(T) measures the work that can be extracted from the system at constant temperature. It is directly related to the partition function as:

$$F_{therm} = -k_B T \ln Q \tag{2.24}$$

At zero temperature, $F(0)=E_1$. As temperature increases, the entropic term $-TS$ makes F more negative [49, 35]. The free energy determines the equilibrium condition and is useful for analyzing phase transitions or stability. In our context, the crossover of F from positive to negative (relative to an arbitrary reference) indicates the temperature above which entropic effects dominate over the zero-point energy.The behavior of F under varying field conditions allows for the assessment of the system's transition tendencies. Because the partition function Z is implicitly dependent on the external fields (E, B, P), the Helmholtz free energy serves as the generator for other thermodynamic variables, ensuring consistency across the entire caloric analysis.

2.5.3 Entropy

Entropy S measures the statistical disorder or the degree of uncertainty in the occupation of the electronic states. The entropy S(T) quantifies the disorder of the electron distribution among the subbands. It is calculated from the temperature dependence of the Helmholtz free energy:

$$S= k_B \ln Q + k_B \beta U \tag{2.25}$$

At T=0, the system is in a pure ground state, so S(0)=0. As temperature increases, higher states become accessible and S grows [50, 93]. When all four levels are equally populated, the entropy saturates at $k_B \ln 4 \approx 1.15\times10^{-4}$ eV/K [11, 93]. In practice, because the level spacings are finite and the barriers are not infinite, the saturation occurs at temperatures well above 800 K for our structures.In this quantum system, entropy is highly sensitive to the energy level spacing. As external fields modify the density of states and the spacing between subbands, the entropy profile exhibits non-monotonic behavior, particularly near the crossings or anticrossings of energy levels induced by hydrostatic pressure.

2.5.4 Heat Capacity

The heat capacity C(T) at constant volume describes how much heat is required to raise the temperature of the electronic system by one kelvin. It is calculated by taking the derivative of the mean energy with respect to temperature. It is the temperature derivative of the mean energy:

$$C_V = \frac{\partial U}{\partial T} = k_B \beta^2 \frac{\partial^2 \ln Q}{\partial \beta^2} \tag{2.26}$$

This expression highlights the variance of the energy distribution. For a discrete system with a few levels, the heat capacity exhibits a characteristic peak known as the Schottky anomaly [11, 49, 55]. This peak occurs when k_BT is comparable to the energy gap between the ground state and the first excited state.These peaks are essential indicators of the system's thermal responsiveness and are found to be tunable via the application of external pressure and field strength.

2.5.5 Magnetocaloric Effect

The magnetocaloric effect describes the change in entropy of a system when an external magnetic field is applied isothermally. This effect is crucial for evaluating the cooling potential of the quantum structures. It is quantified by the isothermal entropy change [86, 85]:

$$\Delta S = S(B \neq 0,T) - S(B = 0,T) \quad (2.27)$$

where S(T,B) is the entropy at magnetic field B and S(T,0) is the entropy at zero field, both at the same temperature. A negative ΔS indicates that the field reduces the disorder whereas a positive ΔS indicates that the field increases the disorder.We compute ΔS for magnetic field sweeps (0–12 T) and also for composition by analogy, though the term "magnetocaloric" is strictly for magnetic fields. In this thesis we focus on the magnetic field case because the Landau diamagnetic term directly modifies the energy levels without altering the potential shape as drastically as the electric field.By utilizing the Maxwell relation, the entropy change can be computed to determine the efficiency of the magnetocaloric cooling cycle [86]. The structural asymmetry and many field perturbations in the MoS_2 and chalcogenide systems allow for the optimization of ΔS_M providing a theoretical base for utilizing these nanostructures in micro-scale refrigeration technologies.

4.7 Material Parameters and Sweep Ranges (Table)

Parameter	Symbol	Value / Range	Unit	Remarks / Ref.
Common constants				
Reduced Planck constant	$\hbar$	1.0546×10^{-34}	J·s	
Elementary charge	e (or q)	1.602×10^{-19}	C	
Vacuum permittivity	ε_0	8.854×10^{-12}	$F \cdot m^{-1}$	
Speed of light in vacuum	c	2.998×10^{8}	$m \cdot s^{-1}$	
Vacuum permeability	μ_0	$4\pi \times 10^{-7}$	$H \cdot m^{-1}$	
Boltzmann constant	k_B	8.617×10^{-5}	$eV \cdot K^{-1}$	
Material parameters – MoS_2				
Zero-temperature bandgap	E_{g0}	1.9	eV	[89]
Bare effective mass	m^*_0	$0.47 \times m_0$	kg	$m_0 = 9.109 \times 10^{-31}$ kg [89]
Varshni coefficient α	α	0.54	$meV \cdot K^{-1}$	[74]
Varshni coefficient β	β	430	K	[74]

Pressure coefficient (bandgap)	$a\_{pressure}$	12	meV·GPa^{-1}	[68]
Pressure coefficient (barrier)	dV/dP	50	meV·GPa^{-1}	[23]
Step pressure coefficient	dV_{step}/dP	2.136×10^{-30}	m^3	scaled from barrier [23]
Refractive index	n_r	4.5	dimensionless	chalcogenides, [87]
Material parameters $As_2(Se_xTe_{1-x})_3$				
Bandgap (Te-rich, x=0)	$E_g(0)$	0.938	eV	[38]
Bandgap (Se-rich, x=1)	$E_g(1)$	2.1	eV	[38]
Quadratic coefficient	c	0.002	eV	[38]
Kane energy	E_P	18.5	eV	interpolated [12]
Composition range	x	0.2 – 0.8	–	sweep variable [38]
Barrier height (x=0.2)	$V_{barrier}$	0.6	eV	[91]
Step height (x=0.2)	V_{step}	0.19	eV	[91]
Deep well depth (x=0.2)	V_{dp}	0.0	eV	[91]
Geometry				
MoS_2 asymmetric well (total length)	L_{total}	28.5	nm	[23]
Left barrier width	L_{b1}	8	nm	
Primary well width	L_{w1}	4	nm	
Secondary well width	L_{w2}	8.5	nm	
Right barrier width	L_{b2}	8	nm	
$As_2(Se_xTe_{1-x})_3$ step well (total length)	L_{total}	57	nm	[13, 56]
Barrier width (left/right)	L_{bar}	20	nm	

Shallow well width	L_{sw}	7	nm	
Deep well width	L_{dw}	10	nm	
Perturbation sweeps				
Electric field (E)	E_x	0, 8, 16, 24 (MoS_2); 0–80 (chalcogenides)	$kV \cdot cm^{-1}$	[61, 111]
Magnetic field (B)	Bx	0, 4, 8, 12 (MoS_2); 0–15 (chalcogenides)	T	[14, 105]
Hydrostatic pressure (P)	P	0, 1, 2, 3	GPa	[68]
Temperature (T)	T	200 – 500 (sweep); base: 200 K	K	[74, 102]
Optical constants				
Dephasing time	T_2	150	fs	[29, 90]
Dephasing energy	$\hbar\Gamma_{21}$	4.4	meV	$\hbar/T_2$
Population relaxation time	T_1	1	ps	[17]
Optical intensity (nonlinear terms)	I_0	1×10^9	$W \cdot m^{-2}$ (1 $MW \cdot cm^{-2}$)	[34, 85]
Sheet carrier density	N_s	5×10^{15}	m^{-2}	[78]
Well width for volume density	L_w (optical)	12.5 (primary well)	nm	$N_v = N_s / L_w$
Refractive index (chalcogenides)	n_r	4.5	–	[87]
Refractive index (MoS_2)	n_r	3.5	–	estimated

Table 2.1 Material parameters and sweep ranges for MoS_2 and $As_2(Se_xTe_{1-x})_3$ quantum wells

CHAPTER 3
Tunable Mid-Infrared Nonlinear Optics in Chalcogenide 1D $As_2(Se_xTe_{1-x})_3$ Step Quantum Wells

3.1 Introduction

Chalcogenide glasses have emerged as promising materials for nonlinear optics. Their broad infrared transparency and large third-order susceptibility make them attractive for frequency conversion [107, 110, 87]. Among them, arsenic chalcogenides of the form As_2Se_3, As_2Te_3, and their alloys $As_2(Se_xTe_{1-x})_3$ offer a unique combination of properties [66, 20, 8],they can be deposited as thin films, their composition can be continuously tuned, and they remain amorphous, which simplifies fabrication relative to crystalline III-V heterostructures.However, the $As_2(Se_xTe_{1-x})_3$ system is particularly interesting because the Se/Te ratio provides a tuning parameter for bandgap and effective mass both. However, without confinement, the intersubband transitions that govern nonlinear response are difficult to engineer.

This chapter focuses on a step quantum well (SQW) geometry built from $As_2(Se_xTe_{1-x})_3$. The well consists of four regions along the growth direction: a left barrier, a shallow well, a deep well, and a right barrier. The step like potential profile helps breaks the inversion symmetry, which is a necessary condition for occurrence of second order nonlinear processes such as second harmonic generation (SHG) [36, 91]. This chapter explores how composition, electric field, and magnetic field tune the optical properties of $As_2(Se_xTe_{1-x})_3$ step quantum wells.The composition parameter x (the selenium mole fraction) varies across the structure, allowing the bandgap and effective mass to be tailored. In addition to composition, we apply a static electric field along the growth direction and an in-plane magnetic field. Both fields modify the confinement potential and therefore the subband energies and dipole matrix elements. Thus, each mechanism produces different shifts blue, red or blue again which allows the device designers to access a wide spectral window with a single material platform [61, 105, 111].

3.2 Composition Effects

The composition parameter x determines the bandgap of the $As_2(Se_xTe_{1-x})_3$ alloy. As x increases from tellurium rich to selenium rich, the bandgap widens and the electron effective mass increases [38]. Both changes affect the confined subband structure.The bandgap Eg(x) widens which makes the electron effective mass m*(x) increase [38, 56]. Both effects shift the energy levels upward.The wavefunctions of adjacent subbands overlap more strongly because the confining potential is less deep. This larger spatial overlap increases the dipole matrix element $|M_{12}|^2$. At x = 0.8 (Se-rich), the heavier effective mass compresses the potential well. This makes the wavefunctions localize more tightly due to which the overlap weakens and therefore $|M_{12}|^2$ drops.

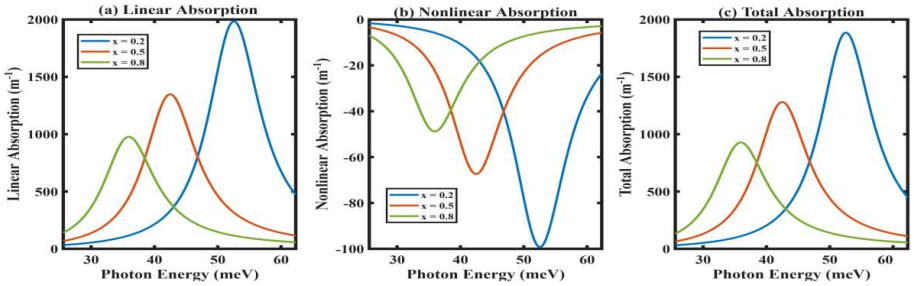

a) b) c)

Fig. 3.1 a) linear absorption coefficient b) Non linear absorption coefficient c) Total absorption coefficient for x = 0.2, 0.5 and 0.8 at F= 5 kV/cm and B= 6T.

Fig. 3.1 shows the total absorption coefficient including the linear and non linear absorption coefficient as a function of photon energy for x = 0.2, 0.5 and 0.8, with fixed electric field F = 5 kV/cm and magnetic field B = 6 T. The peak position shifts from approximately 40 meV at x = 0.2 to about 55 meV at x = 0.8. The peak magnitude, however, decreases from about 2000 cm^{-1} to 800 cm^{-1}. This reduction is explained by the oscillator strength $f \propto |M_{21}|^2 \Delta E_{21} / m^*$. The heavier effective mass further reduces the oscillator strength. Thus, tellurium-rich wells (x = 0.2) give the strongest linear absorption.

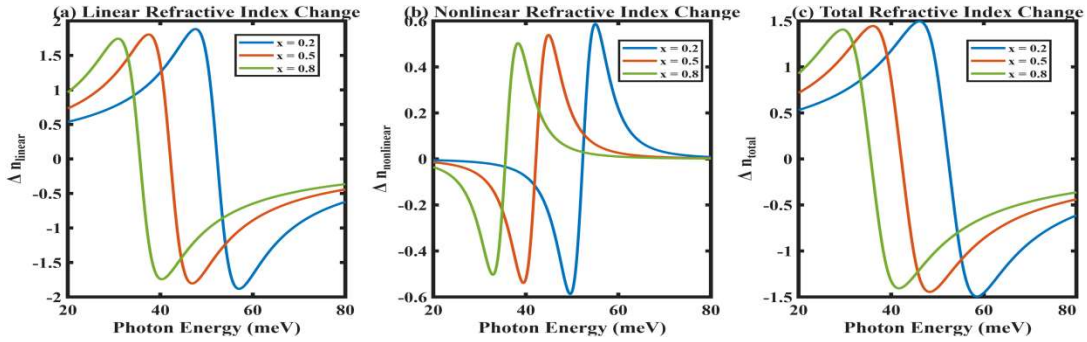

a) b) c)

Fig. 3.2 a) linear refractive index change b) Non linear refractive index change c) Total refractive index change for x = 0.2, 0.5 and 0.8 at F= 5 kV/cm and B= 6T.

Fig. 3.2 shows the total refractive index change which includes linear and non linear terms as a function of photon energy for x = 0.2, 0.5 and 0.8, with fixed electric field F = 5 kV/cm and magnetic field B = 6 T. Just like the absorption coefficient, the refractive index change $\Delta n/n_r$ shows a similar blue shift with x. The linear part $\Delta n^{(1)}$ exhibits the characteristic dispersion: positive below resonance, crossing zero at E_{21}, and negative above resonance. The total change is reduced in magnitude for higher x because $|M_{21}|^2$ is smaller. Thus, the Te-rich composition is therefore preferred for phase-sensitive applications such as modulators.

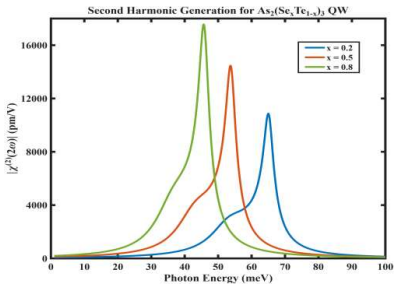

Fig. 3.3 Second harmonic generation (SHG) susceptibility $\chi^{(2)}$ for x = 0.2,0.5,0.8 at F= 5 kV/cm and B= 6T.

The second harmonic generation susceptibility $\chi^{(2)}$ depends on the triple product of M_{12},M_{23},M_{31}. This product is highly sensitive to asymmetry. Such that for x = 0.2, the step potential is relatively shallow and the wavefunctions extend further into the step region, enhancing the overlap between ψ_1, ψ_2 and ψ_3. As x increases, the effective mass rises and the wavefunctions localise more strongly in their respective sub-wells. The overlap decreases, and $\chi^{(2)}$ drops. At x = 0.2, the peak $|\chi^{(2)}|$ is about 1.4×10^{-10} m/V (140 nm/V after conversion) [30]. At x = 0.8, it falls by a factor of nearly three. The resonance positions also blue shift because E_{21} and E_{31} increase with x.

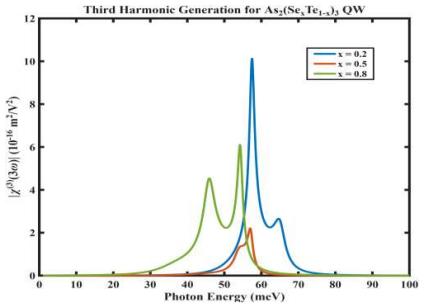

Fig. 3.4 Third harmonic generation (THG) susceptibility $\chi^{(3)}$ for x = 0.2,0.5,0.8 at F= 5 kV/cm and B= 6T.

The third harmonic generation susceptibility $\chi^{(3)}$ follows a similar trend as its second order counterpart. It involves four dipole matrix elements M_{12} M_{23} M_{34} M_{41}. We see the reduction with the increasing x as more pronounced since each additional dipole factor magnifies the localisation effect. For x = 0.2, $|\chi^{(3)}|$ is on the order of 2×10^{-20} m²/V² (or 20×10^{-15} after scaling), which is comparable to values reported for GaAs quantum wells [59]. And then becomes an order of magnitude smaller for x = 0.8,.

In summary, composition tuning offers a way to shift the operating wavelength from the near-infrared (for Te-rich) to the mid-infrared (for Se-rich), but at the cost of reduced nonlinear conversion efficiency. The optimum composition depends on the application: Te-rich wells are best for high-efficiency frequency conversion, while Se-rich wells are suited for longer-wavelength operation where material absorption is low.

3.3 E field effects

The application of an external electric field along the growth direction of the step quantum well adds an additional linear potential term to the Hamiltonian. This tilts the structural symmetry of

the system. This tilting leads to the quantum confined Stark effect which consequently changes the optical properties of the well as field increases [61, 62, 111].

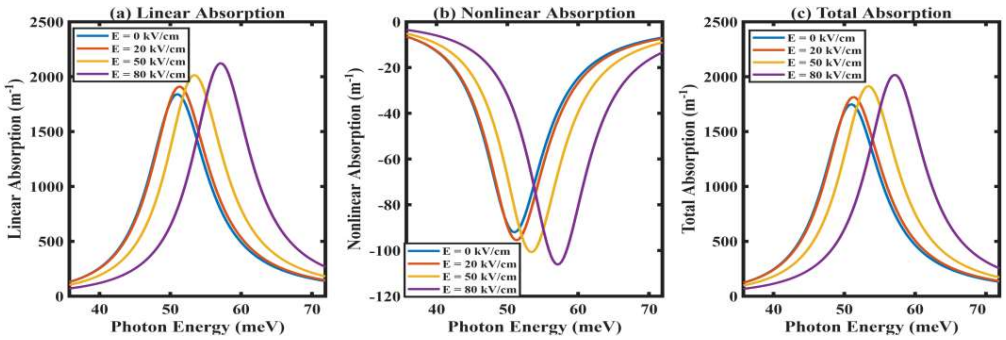

a) **b)** **c)**

Fig. 3.5 a) linear absorption coefficient b) Non linear absorption coefficient c) Total absorption coefficient for F= 0,20,50,80 kV/cm at x = 0.2 and B= 6T.

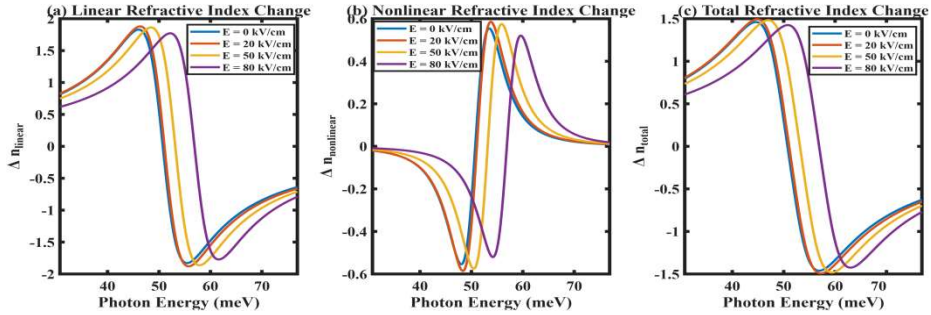

a) **b)** **c)**

Fig. 3.6 a) linear refractive index change b) Non linear refractive index change c) Total refractive index change for for F= 0,20,50,80 kV/cm at x = 0.2 and B= 6T.

The electric field sweeps from 0 to 80 kV/cm. The composition is fixed at x = 0.2 (tellurium-rich), and the magnetic field is 6 T. Increasing the field introduces a redshift in absorption peak. The shift is about 0.025 meV per kV/cm over the low-field range. At higher fields, the shift becomes larger since the Stark effect has a quadratic component as well which becomes more apparent later. The magnitude also decreases with field. At 80 kV/cm, the total absorption is about half of its zero-field value. The refractive index change follows the same trend as absorption. The magnitude of Δn also decreases with increasing field. At zero field, the peak Δn/n_r is about 0.025. At 80 kV/cm, it drops to 0.012. The dispersive shape stays symmetric around resonance. The field does not distort the lineshape.

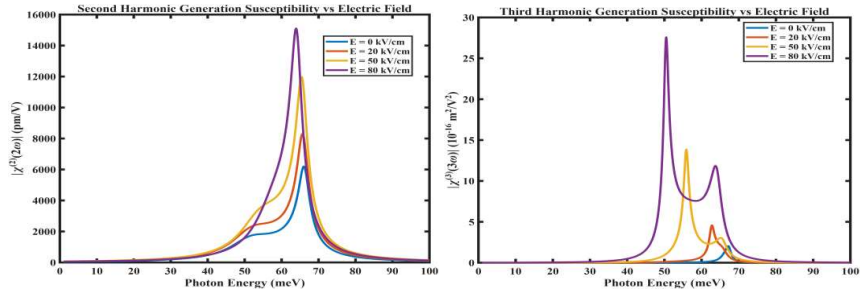

Fig 3.7 Second-harmonic generation susceptibility $\chi^{(2)}$ for F = 0,20,50,80 kV/cm at x=0.2 and B= 6T

Fig 3.8 Third-harmonic generation susceptibility $\chi^{(3)}$ for F = 0,20,50,80 kV/cm at x=0.2 and B= 6T.

The susceptibilities $\chi^{(2)}$ and $\chi^{(3)}$ depend on the triple product $M_{12}\cdot M_{23}\cdot M_{31}$ and four-dipole product $M_{12}\cdot M_{23}\cdot M_{34}\cdot M_{41}$ respectively. As the field increases, M_{12} decreases but M_{23} and M_{31} increase. This results in an increase in magnitude of SHG and THG. SHG spectrum shows two peaks . One at $\hbar\omega = E_{21}$ (one-photon resonance ans the second at $2\hbar\omega = E_{31}$ (two-photon resonance). Both peaks redshift with increasing field and their magnitudes inceases at the same time. At 80 kV/cm, $\chi^{(2)}$ is nearly double the zero-field value. $\chi^{(3)}$ shows three resonance peaks. They correspond to ω, 2ω, and 3ω matching E_{21}, E_{31}, and E_{41} respectively. Field enhances the peaks and shifts them to lower energies.

These results showcase an important design principle for applications that require strong harmonic generation [43, 59]. The applied field enhances the asymmetry already present in the step well, making the nonlinear polarisation larger while also weakening the absorption range.

3.4 B field effects

Applying a magnetic field perpendicular to the growth direction introduces a parabolic term in the Hamiltonian [14, 105]. The parabolic potential (hbar k_y + qB_x z)^2/ 2m* pushes the wavefunction towards the centre. Since the higher states feel the parabolic push more because they are more delocalised, their transition energies increase. This introduces a blueshift. In this study, B field varies from 0 to 15 T while the composition is fixed at x = 0.2, and the electric field is 5 kV/cm.

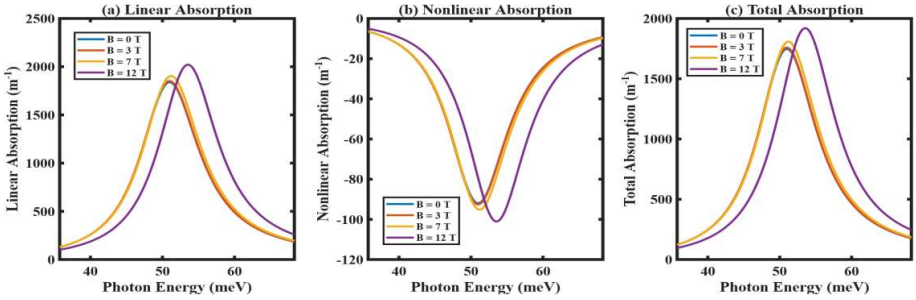

(a) (b) (c)

Fig. 3.9 a) linear absorption coefficient b) Non linear absorption coefficient c) Total absorption coefficient for (B = 0, 3, 7, 12 T) at x=0.2 and F = 5kV/cm

The absorption peak gets blueshifted while the magniotude doesnt chnage much [105, 104]. The shift is about 0.08 meV per tesla. Unlike the electric field, the magnetic field squeezes them toward the centre. The overlap between the ground state and first excited state remains almost constant. So $|M_{21}|^2$ stays roughly the same and the absorption magnitudes stay stable.

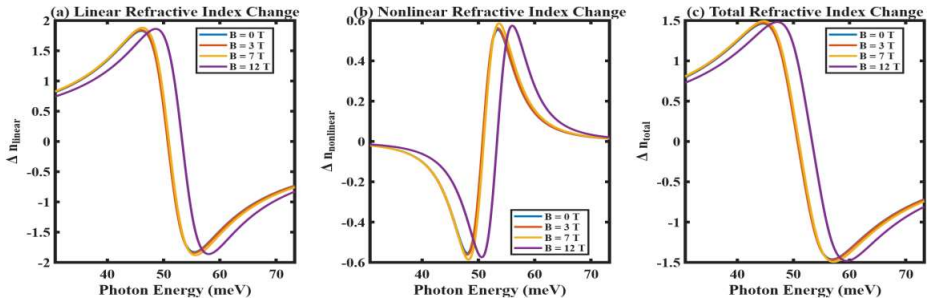

a) (b) (c)

Fig. 3.10 linear refractive index change b) Non linear refractive index change c) Total refractive index change for for (B = 0, 3, 7, 12 T) at x=0.2 and F = 5kV/cm

The refractive index change behaves like the absorption trend for this parameter variation. It also experiences a blueshift. Its magnitude also stays nearly constant. It's peak changes from 0.023 at zero field to 0.022 at 15 T. Magnatic field provied spoectral tuning without the loss of strenght.

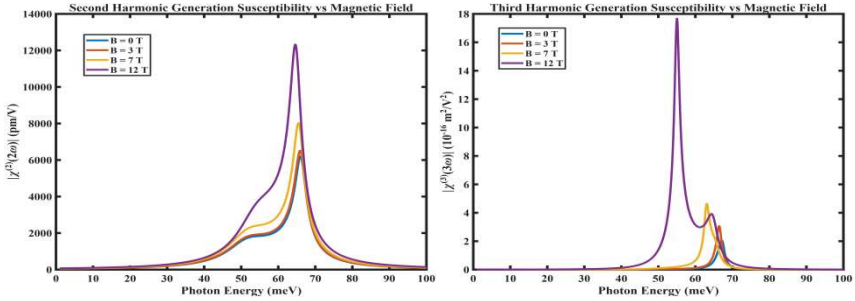

Fig 3.11 Second-harmonic generation susceptibility $\chi^{(2)}$ for for (B = 0, 3, 7, 12 T) at x=0.2 and F = 5kV/cm.

Fig 3.12 Third-harmonic generation susceptibility $\chi^{(3)}$ for (B = 0, 3, 7, 12 T) at x=0.2 and F = 5kV/cm.

The SHG and THG spectrum also blueshifts. The one-photon peak (at $\hbar\omega = E_{21}$) and the two-photon peak (at $2\hbar\omega = E_{31}$) and three-photon peak (at $3\hbar\omega = E4_1$) all moves to higher energy. But their magnitudes drops very rapidly. At 15 T, $\chi^{(2)}$ is about 80% of its zero-field value. Similarly at 15 T, $\chi^{(3)}$ is about 70% of its zero-field value [88].

3.5 Applications

These quantum well structures offer a wide range of practical uses. The tunability demonstrated in this chapter points to several practical applications in the mid infrared region.Their optical properties can be tuned over a wide range using composition, electric fields, and magnetic fields variation and more.

Mid-infrared photonics has many applications. The $As_2(Se_xTe_{1-x})_3$ step quantum well addresses several of them as:

- For frequency converters for mid-IR generation. The SHG and THG susceptibilities are large enough to be useful [73, 30]. For x = 0.2, $|\chi^{(2)}|$ reaches 140 nm/V at zero field and nearly doubles under an applied electric field of 80 kV/cm. The step geometry enhances efficiency through triple-resonance conditions. Thus, Electric and magnetic field tuning allows the converter to track molecular absorption features.
- In case of magneto-optic devices, the magnetic field blue-shifts the response without reducing absorption. This property is useful for devices that require a fixed absorption strength but a tunable wavelength, such as wavelength-selective detectors or filters. The magnetic field tuning keeps maintained amplitude which makes such devices practical.
- Tunable infrared photodetectors [95, 44]. The step well confines electrons and holes. Intersubband transitions can be designed to match specific detection wavelengths. Applying fields shifts the response, allowing the detector to track different wavelengths. Chalcogenide materials have high room-temperature operation potential, thus pretty handy for such applications.

In conclusion, the step quantum well based on $As_2(Se_xTe_{1-x})_3$ offers a versatile platform for tunable mid-infrared nonlinear optics. Composition sets the baseline wavelength. The electric field provides continuous red-shift tuning and enhances harmonic generation. The magnetic field provides blue-shift tuning with stable absorption. Applied together, they allow the optical response to be adapted to a wide range of applications.

CHAPTER 4

Thermodynamic study of $As_2(Se_xTe_{1-x})_3$ Step Quantum Wells under the variation of Composition, Electric Field and Magnetic Field.

4.1 Introduction

Recent advancements in the field of nanomaterials have highlighted the potential of low dimensional semiconductor nanostructures [11, 49, 35], such as quantum dots and quantum wires, for the development highly efficient and tunable devices. These structures depends on quantum confinement to affect their behavior, leading to breakthroughs in applications of optoelectronics, photovoltaics, quantum computing, and bioimaging.

Understanding the thermodynamic properties of these semiconductor nanostructures is an eessential problem in modern materials science. Quantities such as entropy, specific heat capacity, Helmholtz free energy, and mean energy provides us a critical insights into the thermal stability and operational limits of these nanoscale devices [11, 50, 93].

Historically, the thermodynamic behavior of simple quantum wells using basic parabolic, square, or Gaussian confinement potentials has been extensively studied [11, 49, 51]. However, there remains a significant gap in our understanding of complex, composition-tunable ternary systems.

The usage of ternary chalcogenide alloys, specifically $As_2(Se_xTe_{1-x})_3$, presents a unique opportunity for bandgap engineering applications[38, 56, 13]. Therefore, this chapter aims to theoretically investigate the low as well as high temperature thermodynamic behavior of an $As_2(Se_xTe_{1-x})_3$ step quantum well. Apart from standard thermodynamic quantities i.e mean energy, heat capacity, Helmholtz free energy, and entropy, this study also explores the magnetocaloric effect (MCE) by evaluating the isothermal entropy change induced by external fields [86, 85, 78].

To achieve this, we solve the one-dimensional Schrödinger equation using the finite element method (FEM) to obtain the system's eigenenergies. These energy levels are subsequently used to construct the canonical partition function, from which all thermodynamic properties are derived within the canonical ensemble framework. The investigation systematically evaluates the impact of three primary tuning parameters: (a) Alloy composition(x), (b) Electric field(E) and (c) Magnetic field(B)

4.2 Mean Energy

The mean energy of a quantum system is the average energy stored in the electron gas at a given temperature. We compute the mean energy from the canonical partition function.Here, Ei are the eigenenergies from the Schrödinger equation, kB is the Boltzmann constant, and the sum runs over the four lowest subbands.

At lower temperatures, the system already occupies the ground state and the mean energy closely tracks the zero-point energy of the structure [11, 49]. As the temperature increases the

thermal excitations populate higher energy states and causes the mean energy to rise accordingly.

A magnetic field raises all subband energies through diamagnetic confinement [50, 70]. The behavior at low temperatures is heavily influenced by the field magnitude. At low temperatures, the mean energy is higher because E1 is higher. But at higher temperatures, the thermal energy k_B Tbegins to dominate over the field-induced energy shifts. And hence at higher tempuratures, the occupation of multiple levels becomes comparable across all field values which causes the field-dependent mean energy curves to converge [11, 49].

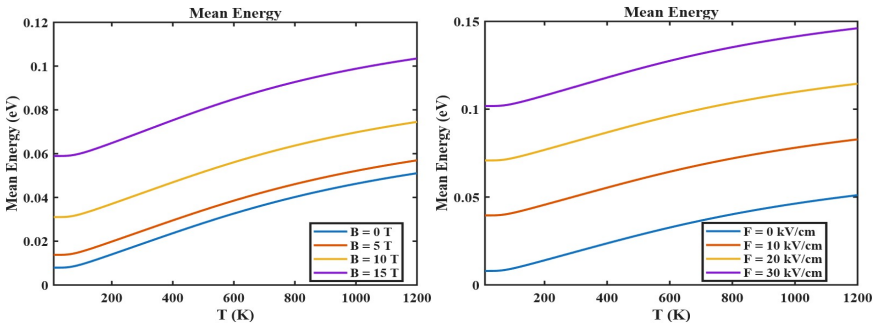

Fig 4.1 Mean energy versus temperature for B =0,5,10,15 T at x =0.2 and F=0.
Fig 4.2 Mean energy versus temperature for F = 0,10,20,30 kV/cm and x=0.2 and B=0.

51

An applied electric field raises all subband energies through the Stark shift [61, 72]. This exerts a strong influence on the mean energy. The electric field breaks the spatial symmetry of the step well and shifts the lowest eigenstate into a higher energy configuration. The ground state rises more than the excited states in an asymmetric well. So E_{21} decreases. This increases the effective zero-point energy. At low temperatures, the mean energy is higher because E_1 is higher. the separation between the mean energy curves at different electric field strengths remains approximately constant. And hence The electric field curves are nearly parallel to the zero-field curve but shifted upward and with similar shape.

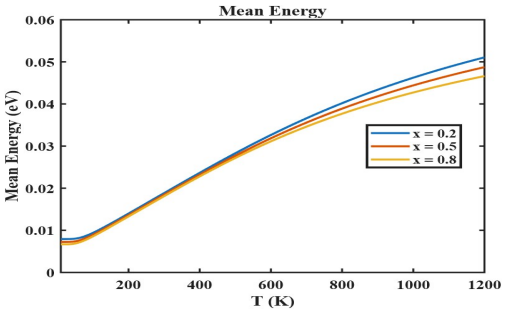

Fig. 4.3 Mean energy versus temperature for x = 0.2, 0.5, 0.8 at F=0, B=0.

The variation of the selenium mole fraction (x) introduces a distinct modulation of the mean energy. The mean energy decreases consistently with increasing selenium composition across all temperatures [38, 56]. The selenium fraction x changes the effective mass. A heavier effective

mass reduces the kinetic confinement energy and consequently lowers the subband energy levels. At low temperatures, where the system is highly sensitive to the ground-state energy, the composition-dependent mean energy variations are distinctly separated. However, as the temperature rises sufficiently high, the thermal energy exceeds the energy spacing between the quantum levels. this causes the composition-dependent curves to gradually converge.

4.3 Specific Heat Capacity

The specific heat capacity tells us how much energy the system absorbs when the temperature rises by one degree. The specific heat capacity of our quantum well shows a very clear pattern. It rises to a peak and then falls as temperature increases. This is known as a Schottky anomaly [11, 49, 55]. At very low temperatures, electrons stays in the ground state. Because they cannot move up, the heat capacity remains small [11, 17]. When the thermal energy is enough to push electrons into the first excited state, the heat capacity quickly goes up. At higher temperatures, the electrons spread out evenly across all the available energy levels. When this happens, the system absorbs less heat per degree of temperature change, and the curve falls back down.

We compute the heat capacity from the mean energy.An electric field reduces E_{21}. So the Schottky peak shifts to lower temperatures [72]. The electric field pushes all the energy levels up together through the Stark effect. Because the energy gap between the lowest states stays mostly the same, the thermal transitions do not change, and the heat capacity remains steady. Consequently, it barely changes the height or position of the heat capacity peak.

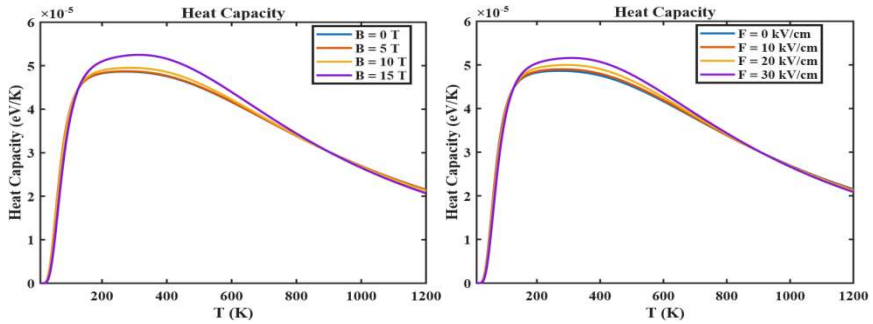

Fig. 4.4 Heat capacity for B = 0,5,10,15 T at x= 0.2 and F=0 kV/cm.
Fig. 4.5 Heat capacity for F = 0,10,20,30 kV/cm at x= 0.2 and B=0 T.

The heat capacity peak shifts to higher temperatures when an in-plane magnetic field is applied [70, 50]. the magnetic field adds a harmonic shape to the well's potential. This changes the spacing between the energy levels in an uneven way. It actually enhances the thermal activation of the states in that specific temperature range. The peak height stays almost constant since M_{21} does not change much. At very high temperatures, the magnetic field stops mattering much, and all the curves merge together.

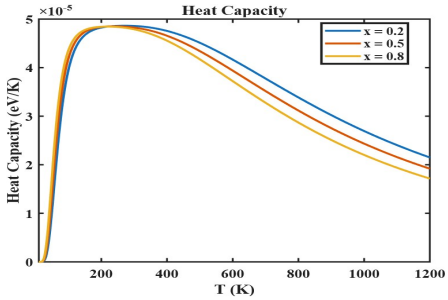

Fig. 4.6 Heat capacity for x = 0.2, 0.5, 0.8 at F=0, B=0.

Changing the alloy composition has the strongest overall effect on the heat capacity [38, 56]. As we increase the selenium content, the peak drops in height. The peak also shifts to a lower temperature and gets wider. the Schottky peak occurs at about 340 K for x = 0.2 and 280 K for x = 0.8 [55]. It is worth noting that this composition trend is steady and monotonic. At high temperatures (above 600 K), all composition curves converge.

4.4 Helmholtz Free Energy

The Helmholtz free energy represents a balance between the system's internal energy and its thermal disorder (entropy). . At very low temperatures, there is aalmost no thermal disorder. Because of this, the free energy starts as a small positive number that closely matches the ground state energy of the system [11, 49]. However, as the temperature rises, the entropy tincreases and pulls the free energy downward into negative values. This steady, continuous drop with rising temperature is a universal feature of quantum systems finding thermal equilibrium. We compute F directly from the partition function. Changing the selenium to tellurium ratio has a major impact on the free energy across all temperatures. For tellurium-rich wells (x=0.2), the ground state energy is higher [38]. So F is bighest at a higher value at low temperatures. It has a lighter effective mass and a higher starting ground-state energy. As the system heats up, this lighter mass also allows for more thermal disorder (higher entropy), which accelerates the downward plunge of the free energy curve. Even at extremely high temperatures, the free energy curves for different compositions do not merge.

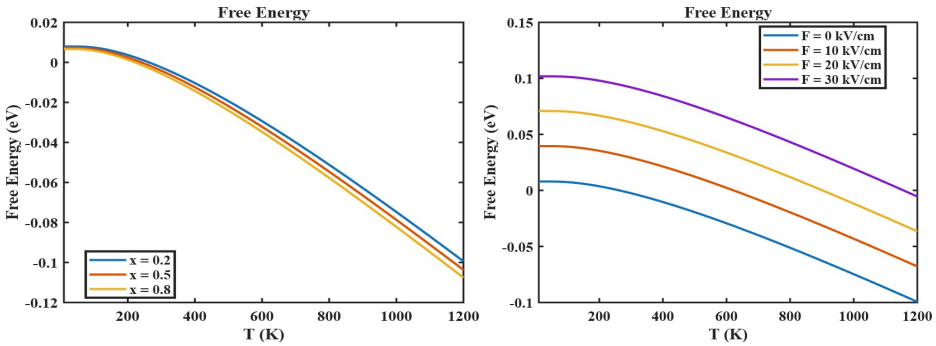

Fig. 4.7 Free energy for x = 0.2, 0.5, 0.8 at F=0 kV/cm, B=0T.
Fig. 4.8 Free energy for F = 0,10,20,30 kV/cm at x=0.2 and B=0T.

An electric field raises all subband energies, especially the ground state [61, 72]. Because the electric field pushes the ground-state energy higher via the Stark effect, the starting free energy at low temperatures is substantially higher when the field is turned on. As the temperature rises, the free energy drops, but it drops at almost exactly the same rate regardless of the field strength. This happens because the electric field does not really change the system's entropy.

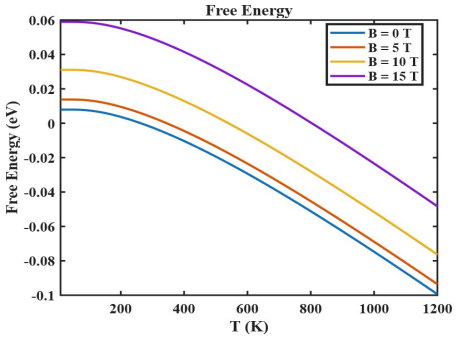

Fig. 4.9 Free energy for B = 0,5,10,15 T at x = 0.2 and F=0 kV/cm.

A magnetic field also raises all subband energies [50, 86]. But the increase is smaller than for the electric field. Increasing the magnetic field produces an almost parallel upward shift in the free energy curves. The zero-field curve crosses into negative values first, while the highest magnetic field curve stays positive the longest. The magnetic field gives a gentle, clean shift without changing the shape much.

4.5 Entropy

The entropy of a quantum-confined system measures its thermal disorder. At absolute zero temperature, the entropy is zero because the electrons are all in the ground state [11, 93]. As the temperature increases, thermal energy excites the electrons, and reaches to more eigenstates and causing the entropy to rise. At very high temperatures, the entropy begins to approach a saturation value. This saturation happens when the electrons have enough thermal energy to spread almost equally across all the energy states in the system.We compute entropy from the partition function. The composition of the alloy has a permanent effect on the system's entropy. Systems with lower selenium content (x = 0.2) consistently exhibit the highest entropy across the entire temperature range [38, 56]. This occurs because the lighter effective mass of this composition creates a higher and more spread out set of eigenstates. Importantly, these composition differences do not converge even at elevated temperatures up to 1200 K.

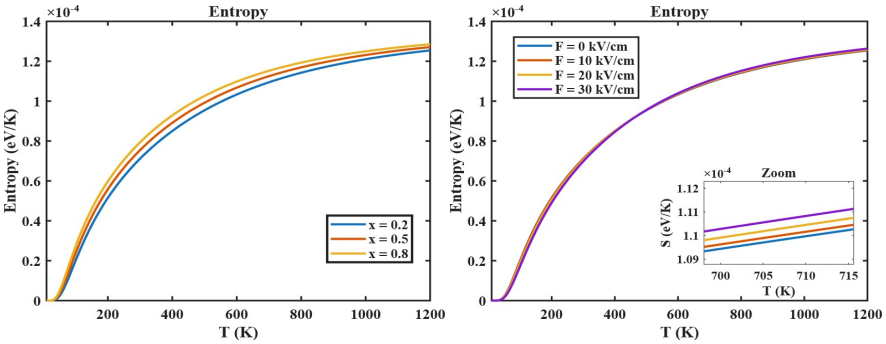

Fig. 4.10 Entropy for x = 0.2, 0.5, 0.8 at F=0 kV/cm, B=0T.
Fig. 4.11 Entropy for F = 0,10,20,30 kV/cm at x = 0.2 and B = 0T.

The response of entropy to an applied electric field is remarkably weak [72, 71]. Whether the field is 0 kV/cm or 30 kV/cm, the entropy curves lie perfectly on top of one another from 0 K all the way to 1200 K. This insensitivity demonstrates that the electric field acts essentially as a rigid shift of all eigenenergies through the Stark effect, leaving the inter-level spacings unchanged [72, 61]. This is highly advantageous for device applications becuase it allows electrical tuning without disrupting the thermal stability of the structure.

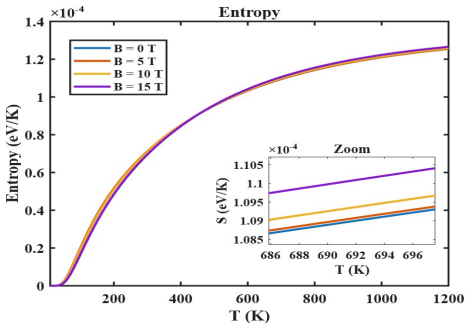

Fig. 4.11 Entropy for F = 0,10,20,30 at x = 0.2 and F = 0 kV/cm.

Similar to the electric field, the magnetic field also has very little effect on the entropy [50, 78]. Between 150 K and 400 K, applying a strong magnetic field causes a very slight decrease in the entropy. This happens because the magnetic field adds a confinement term that slightly widens the gaps between the energy levels. At high temperatures, all curves converge to the same saturation value.

4.6 Magnetocaloric Effects

The magnetocaloric effect (MCE) describes the entropy change of a system under the infuence of magnetic field [86, 85]. For the $As_2(Se_xTe_{1-x})_3$ step quantum well, the MCE is evaluated through the isothermal entropy change $\Delta S = S(B) - S(0)$.

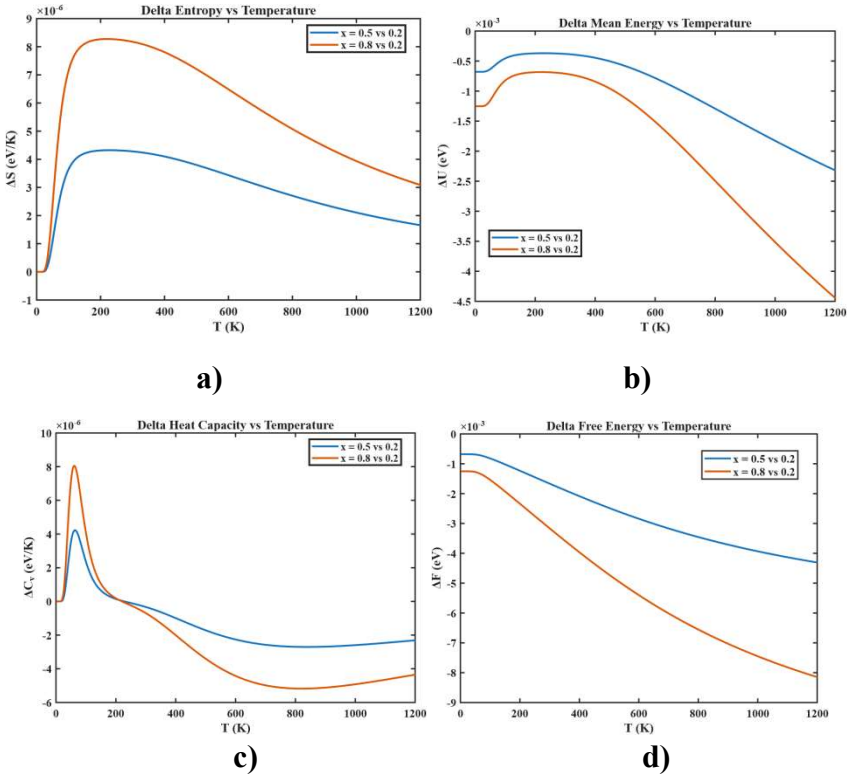

Fig. 4.12 Magnetocaloric effect for (a)Entropy change ΔS, (b) Mean energy change ΔU (c) Heat capacity change ΔC_v and (d) Helmholtz free energy change ΔF.

Even without a magnetic field, changing the composition of the quantum well acts as a magnetocaloric response. This indicates that increasing the Se fraction reduces the intersubband level spacings through heavier effective mass. Because the thermally accessible states are packed closer together, they become more equally populated at intermediate temperatures.Hence it shows positive shift in configurational entropy. It shows that structural tuning can change the system's thermal capacity.

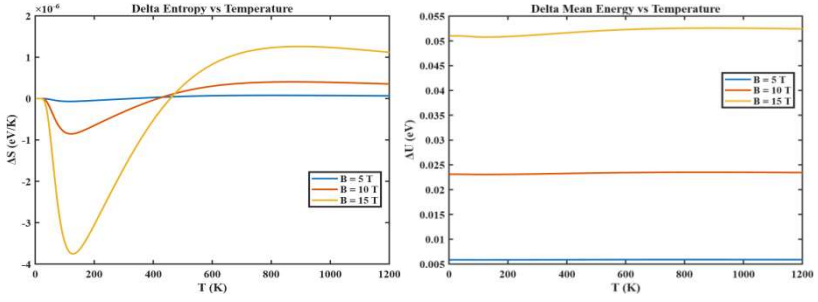

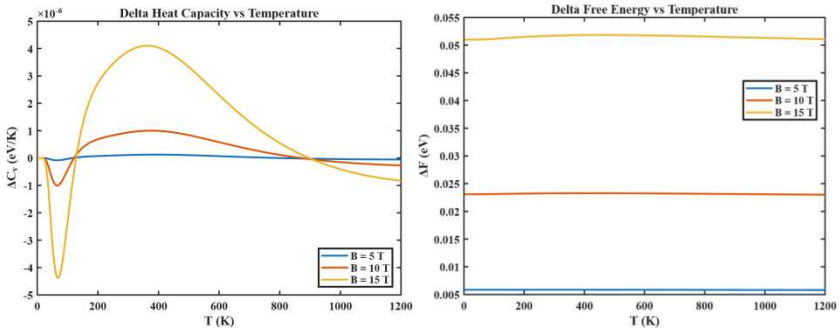

c) d)

Fig. 4.13 Magnetocaloric effect for (a)Entropy change ΔS (b) Mean energy change ΔU (c) Heat capacity change ΔC_v and (d) Helmholtz free energy change ΔF for B= 5,10,15 T.

At low temperatures, applying the magnetic field produces a conventional magnetocaloric effect [85, 86]. The entropy change ΔS = S(B) − S(0) is negative at low temperatures, reaches a minimum around 100–200 K, but then crosses it through zero and gets positive at temperatures above approximately 400–600 K. At low tempurature the diamagnetic confinement term pushes the energy levels further apart [85, 50], effectively "stiffening" the energy spectrum. At high temperatures, the same field-induced broadening of the total energy spread creates a wider phase space for thermal occupation, causing the entropy to exceed its zero-field value [86, 78].

4.7 Applications

The thermodynamic behaviour of the $As_2(Se_xTe_{1-x})_3$ step quantum well, particularly its sensitivity to composition and external fields suggests several practical device-oriented applications. The tunability demonstrated in the previous sections can be exploited across thermoelectric, calorimetric, cryogenic, and quantum technology domains.

Calorimetric Sensing : The specific heat capacity of the quantum well exhibits a distinct Schottky peak. This peak shifts in position and amplitude with both composition and magnetic field. Since the peak is sensitive to composition and magnetic field, the structure can be utilized effectively in high-precision calorimetric sensing. Such sensors are capable of detecting minute changes in thermal activation within specialized nanoscale environments [11, 55, 96].

Thermoelectric Devices : The strong composition dependence of mean energy and entropy suggests that the Se/Te ratio can be used to optimise the Seebeck coefficient and thermal conductivity [100]. By grading the composition along the growth direction or across individual wells, structures with tailored thermoelectric responses can be made for energy harvesting or solid state cooling applications.

CHAPTER 5

Far Infrared and Terahertz Optical Tunability of MoS_2 Asymmetric Quantum Wells Under Multi Field Perturbations

Introduction

The optical properties of an asymmetric quantum well constructed from molybdenum disulfide MoS2 material parameters show unique optical sensitivities [89, 58, 108]. This study systematically investigates effects of four external perturbations, i.e. electric field, magnetic field, hydrostatic pressure, and temperature, all applied simultaneously [23, 25, 18]. One perturbation is varied in strenght while othe kept constant at non-zero values. Each perturbation produces distinct and sometimes opposing trends in absorption, harmonic generation, and refractive index.

Absorption Coefficient

An applied electric field induces a quantum confined Stark effect. This leads to a clear redshift in absorption peak [61, 62, 111]. This happens because the ground state goes low fatser than excited states and subband spacing decreases. In the case of magnetic field, the parabolic confinement stiffens the potential and widens the subband gap.

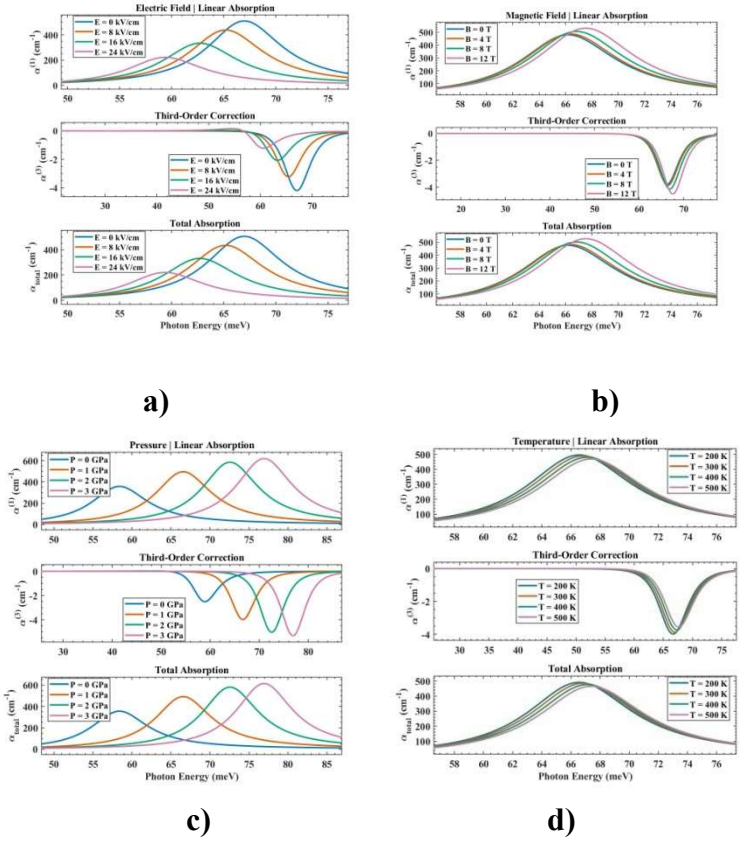

Fig. 5.1. Linear $\alpha^{(1)}$ (top), third order $\alpha^{(3)}$ (middle), and total α_{total} (bottom) absorption vs. photon energy for a) E, b) B, c) P, d)T perturbations respectively.

This induces a blueshift in absorption coeffeicent and increases the peak as well [14, 105]. Hydrostatic pressure shows the most dominant spectral shift among all perturbations and creates a steep blueshift. It increases the barrier height and electron effective mass which narrowislevel spacings relative to the primary well but lifts the higher subbands faster than the ground state [68, 23]. The temperature change gives a small blueshift. The bandgap shrinks and effective mass reduces, causing wavefunctions to spread whgich causes the magnitude to decrease [74, 102].

Second Harmonic Generation (SHG)

The SHG susceptibility $\chi^{(2)}$ often follows trends opposite to those of linear absorption. Under an increasing electric field, the SHG spectral peaks move to lower energies, yet the total magnitude nearly doubles [43, 30]. This counterintuitive effect arises because the field enhances spatial overlaps between specific subband pairs (e.g., ψ_2-ψ_3 and ψ_3-ψ_1).

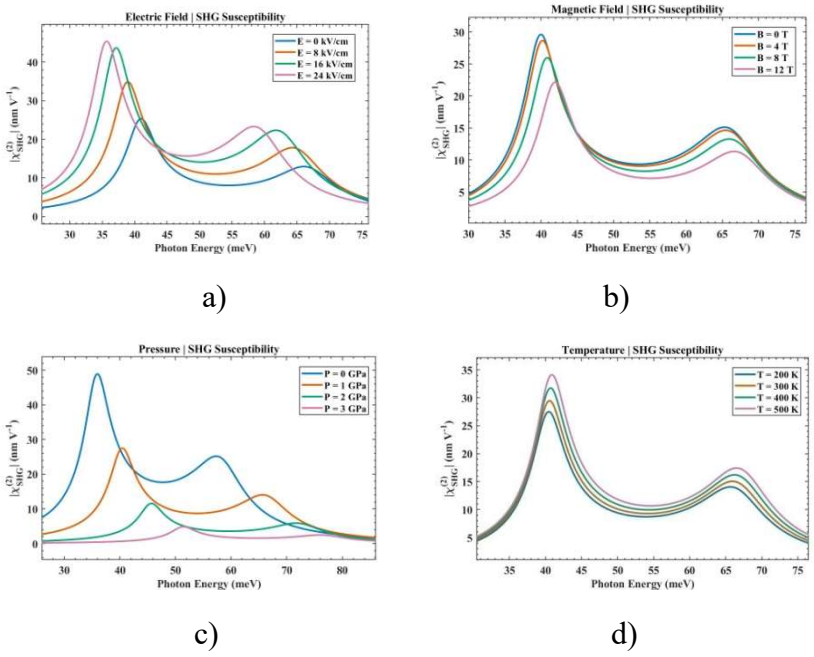

Fig. 5.2. SHG vs. photon energy for a) E, b) B, c) P, d)T perturbations respectively.

The magnetic field causes a blueshift in the SHG spectra but steadily reduces its overall magnitude [88, 15]. This pushes all wavefunctions toward the well center, reducing the overall spatial asymmetry needed for a strong second-order response. Hydrostatic pressure collapses $\chi^{(2)}$ almost entirely (by nearly 90%) [25]. The pressure localizes individual wavefunctions tightly within separate sub-wells, and destroysthe intersubwell spatial overlap required for the dipole product. Temperature, however, increases $\chi^{(2)}$ [64]. This is becuase of the spreading of wavefunctions from a reduced effective mass improves the necessary intersubwell overlaps.

Third Harmonic Generation (THG)

The trends for the THG susceptibility, $\chi^{(3)}$, largely mirror those of SHG and by the same mechanisms. The electric field more than doubles $\chi^{(3)}$, the reason being an enhanced coupling across four subbands [59, 106]. It also shifts the peaks toward lower photon energies.

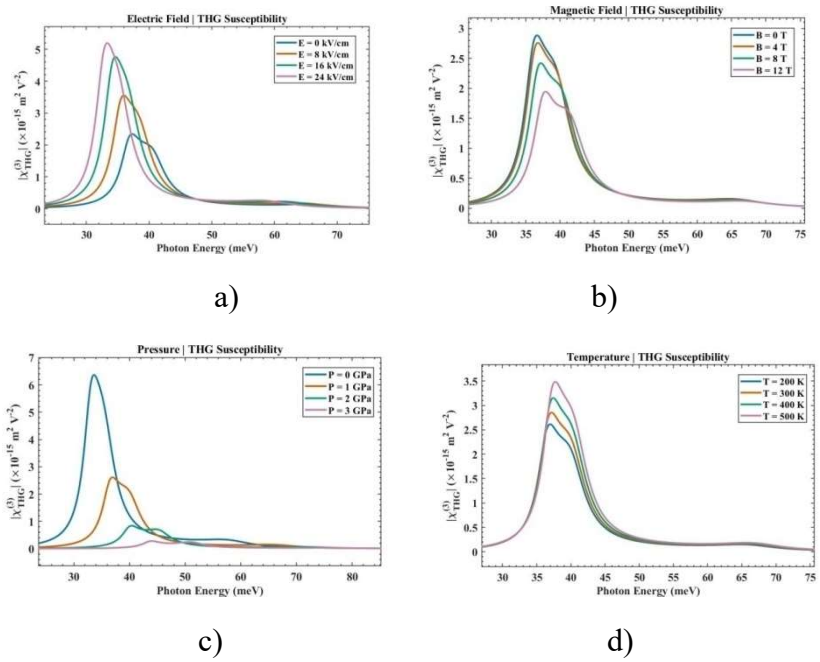

Fig. 5.3. THG vs. photon energy for a) E, b) B, c) P, d)T perturbations respectively.

Magnetic field moves the THG spectra to higher energies and suppresses its magnitude. Hydrostatic pressure exerts extreme suppression of the THG magnitude alongside a spectral blueshift. The value drops by over 95% across the pressure sweep as wavefunction localization breaks all four required couplings [25]. Temperature again increases $\chi^{(3)}$ with a subtle rightward spectral shift [64].

Refrective Index

The total refractive index change (Δn_total) displays a dispersive lineshape and it closely tracks the absorption resonance [2, 19]. The linear, third-order, and total refractive index change Δn spectra consistently mirror the behavioral trends, directions, and spectral shifts observed in the absorption spectra.

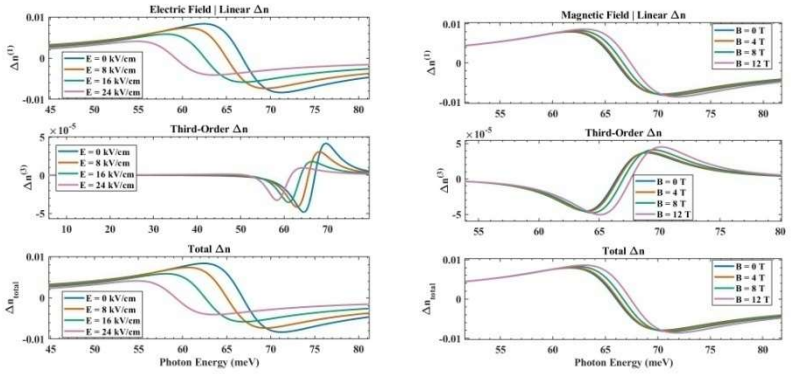

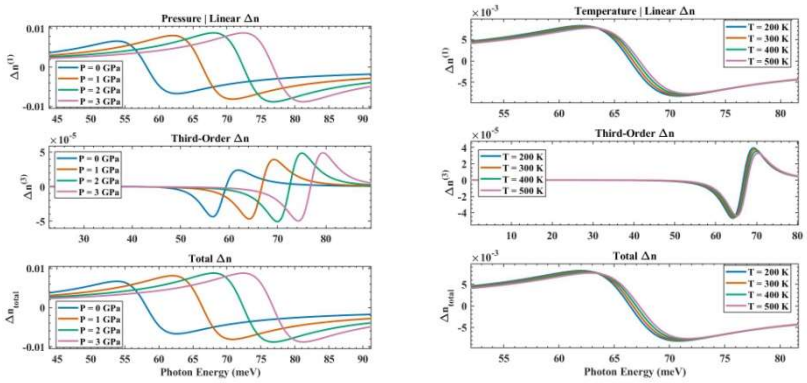

c) d)

Fig. 5.1. Linear (top), third order (middle), and total (bottom) refractive index change vs. photon energy for a) E, b) B, c) P, d)T perturbations respectively.

With an increasing electric field, the refractive index spectrum shifts down to lower photon energies and shows a notable decrease in peak magnitude [61, 104]. It blueshifts under a magnetic field while experiencing an increase in peak magnitude. Hydrostatic pressure induces a strong blueshift [68]. Under temperature variation, refrective index shifts slightly to higher energies, while the magnitude of the refractive index change slowly decreases.

Applications

The collective trends shows that an MoS_2 asymmetric quantum well is versatile for field tunable optical usage across the far-infrared and terahertz spectrum (60–80 meV). The electric field enables a switch like behavior. At low field strenght, the linear absorption dominates. While at high field strenght , nonlinear responses (SHG/THG) are strongly enhanced and absorption is suppressed. This is ideal for low-power modulators and frequency converters [16, 95].

46

The magnetic field blueshifts the peak and increases the magnitude of linear absorption. But it suppresses $\chi^{(2)}$ and $\chi^{(3)}$. This suggests applications in magnetically tunable terahertz detectors or filters where one wishes to shift the operating wavelength upward without compromising absorption strength.

Since pressure induces the largest spectral shift, it can be used for coarse, wide-band spectral positioning to lock the device into a specific terahertz target band [68, 25]. This can be exploited as pressure-tunable narrowband terahertz sensors or spectrometers

As the temperature rises, the linear absorption decreases, but the higher order nonlinear susceptibilities $\chi^{(2)}$ and $\chi^{(3)}$ actually increase. This is advantageous for devices that operate over a range of ambient temperatures since the nonlinear response actually improves with heating, while the resonance position remains nearly stable.

The paper also implies that these perturbations can be applied simultaneously. This opens the door for multi-field control. For example, using an electric field to enhance nonlinearity while

using pressure to coarsely set the operating wavelength, and a magnetic field for fine-tuning. This give a great control over the functionality of device.

All of this tunability is realized in MoS_2 which is a non-toxic, earth-abundant, and environmentally safer alternative to conventional GaAs-based quantum wells [58, 89]. This makes the proposed devices not only functionally competitive but also sustainable and scalable for future terahertz communication, imaging, and spectroscopy systems.

CHAPTER 6

Thermodynamic Properties of MoS_2 Asymmetric Quantum Wells under Temperature, Pressure, Electric and Magnetic Fields

Introduction

In a quantum well, electrons are confined in a small space. Their energy levels become discrete [7, 65]. These discrete levels determine how the system stores heat, how its entropy changes, and how it responds to temperature changes. Its thermodynamic properties are computed from the electronic energy levels. By solving the one-dimensional effective mass Schrödinger equation with the finite element method, the energy states are extracted .The four lowest lying states E_1, E_2, E_3, E_4 are treated as a finite level system. These eigenvalues are then used in a partition function formalism to derive fundamental thermodynamic potentials [35, 53], like internal energy (U), Helmholtz free energy (F), entropy (S), and the constant-volume electronic heat capacity (C) over a wide temperature range up to 800 K. This approach follows the standard statistical mechanics of a canonical ensemble [11, 49, 35].

Electric field effects

An electric field tilts the potential. It pulls the ground state down faster than the excited states [61, 72]. This reconfiguration in potential directly changes the canonical partition function and changes the energy distribution of the system. This changes the thermodynamic response in a systematic way.

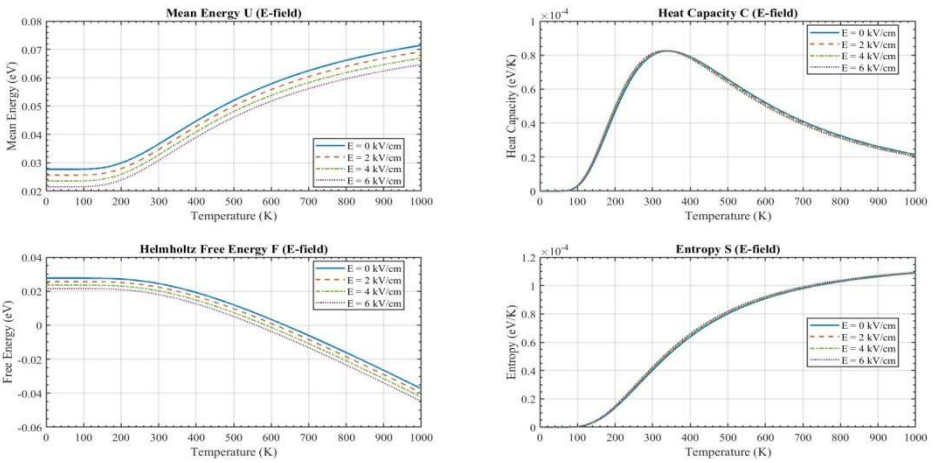

Fig. 6.1. Electric Field Effects for Mean Energy, Heat Capacity, Helmholtz Energy and Entropy.

The peak position of the heat capacity is dependent on the electric field. It shifts toward lower temperatures as E filed increases [72]. The energy gap between the ground state and the first excited state shrinks, which means the thermal excitation happens at a lower temperature [72,

71]. This downward shift occurs at a steady linear tuning rate. It demonstrates a clear electrical control over the thermal maximum.

Entropy also gets reshifted. At very low temperatures, it is zero. At high temperatures, it saturates to a constant value depending uponthe number of available states. The electric field does not change that saturation value much. But it does shift the temperature at which entropy rises most steeply. For the Helmholtz free energy, the system shows a redshift and weak positive curvature at room temperature [35, 78].

Magnetic field effects

The application of a magnetic field adds a quadratic vector potential term to the electron Hamiltonian, which is lic term [50, 70]. This magnetic term increases the stiffness of the quantum potential and forces the electronic wavefunctions closer together, which pushes the entire energy spectrum upward. This magnetic widening of the subband gaps directly impacts the thermodynamic response.

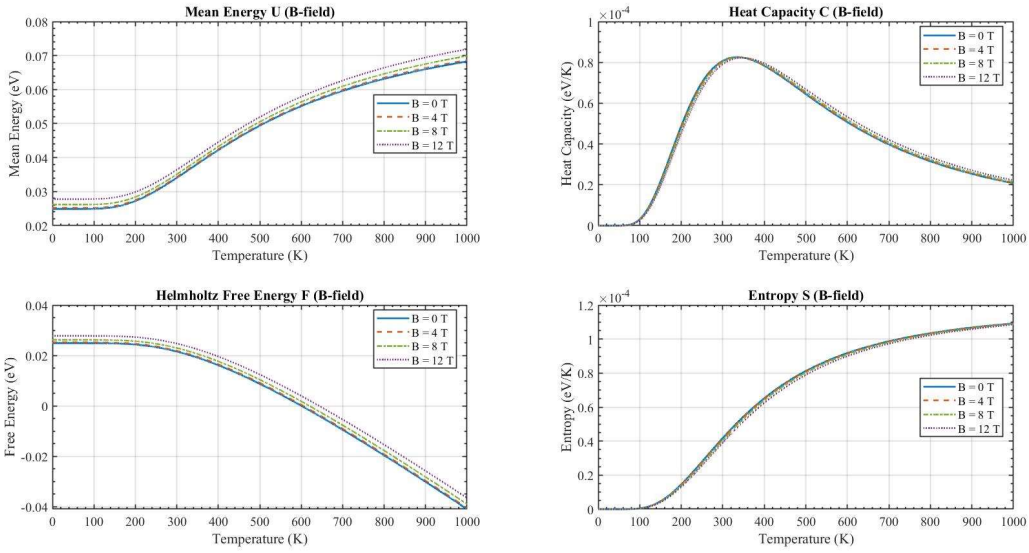

Fig. 6.2. Magnetic Field Effects for Mean Energy, Heat Capacity, Helmholtz Energy and Entropy.

First, the heat capacity peak shifts toward higher temperatures [55, 35]. Then, the free energy curvature at room temperature is negative, which means the field lowers the free energy slightly. The entropy also shows a rightward shift [50, 54]. The steepest part of the entropy curve moves to higher temperatures as the field grows.

Pressure effects

Hydrostatic pressure is the most dominant perturbation in this study. Pressure compresses the crystal lattice of the MoS2 quantum well, which changes the bandgap via deformation potential [68, 48]. This changes both the carrier effective mass and barrier height. These structural changes increase the subband energy gaps substantially.

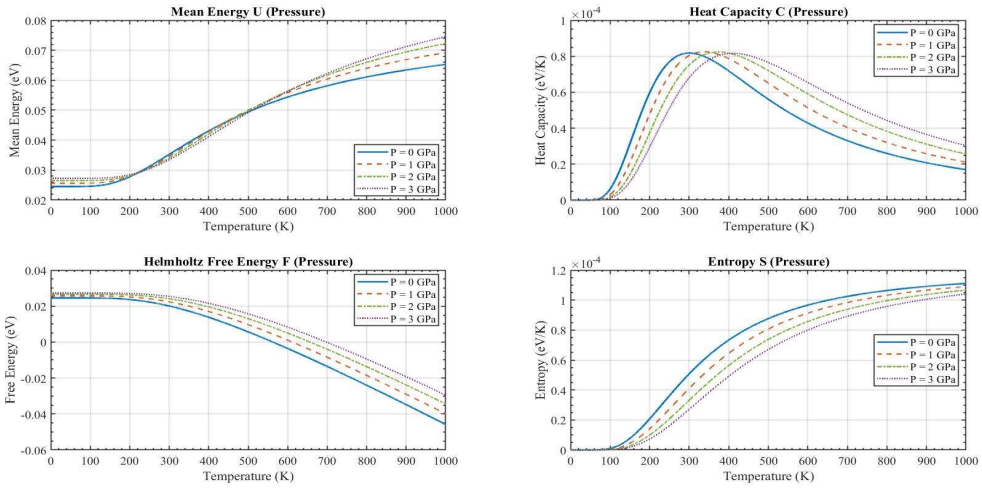

Fig. 6.1. Effects for Mean Energy, Heat Capacity, Helmholtz Energy and Entropy.

The heat capacity peak shifts to much higher temperatures as pressure increases. The tuning rate is about twenty times larger than for the magnetic field and thirty-six times larger than for the electric field [53]. The ground-state energy exhibits a steep positive slope, and the free-energy curves show a strong positive curvature at room temperature [53, 68].

CHAPTER 7

CONCLUSION

7.1 Conclusion

A recurring observation in the literature is that most theoretical studies of quantum well nonlinear optics examines a single perturbation occurring in isolation. However, practical devices rarely operate under such idealised conditions. A working infrared modulator or terahertz frequency converter functions in an environment where temperature fluctuates, fabrication processes introduce residual strain, and applied electric fields coexist with stray magnetic fields. Examining each influence separately therefore gives an incomplete picture. The primary motivation for this work was to construct a unified framework that treats all four major perturbations electric field, magnetic field, hydrostatic pressure, and temperature simultaneously and to apply it to two material systems that have received relatively little attention in the quantum well community.

The choice of $As_2(Se_xTe_{1-x})_3$ and MoS_2 was guided by both practical and scientific considerations. Conventional quantum well research has long relied on GaAs and InP. These materials perform well, but they carry significant disadvantages in terms of toxicity, supply chain vulnerability, and fabrication cost. The chalcogenide alloy and the transition metal dichalcogenide examined here avoid most of those problems. More importantly, both possess optical nonlinearities large enough to be competitive in the mid-infrared and terahertz regimes, and neither had been studied in the specific quantum well geometries investigated here. For $As_2(Se_xTe_{1-x})_3$, the intersubband optical properties of step wells had never been reported as a function of composition. For MoS_2, the far-infrared and terahertz intersubband regime was entirely unexplored. These were substantive open questions, not incremental gaps.

The computational pipeline rested on three connected components. The one-dimensional Schrödinger equation with a position-dependent effective mass was solved using the finite element method in COMSOL Multiphysics. The mesh density was sufficient to resolve wavefunction variations at sub-nanometre scales. The resulting eigenenergies and envelope functions were then used in the density matrix formalism to compute linear and nonlinear absorption coefficients, refractive index changes, and second- and third-order harmonic susceptibilities. The same eigenenergies were also used in the canonical partition function to extract thermodynamic quantities. Running all three modules on identical eigenvalue sets for every parameter combination ensured internal consistency across the optical and thermodynamic outputs.

For $As_2(Se_xTe_{1-x})_3$, the selenium mole fraction x proved to be a tuning parameter with a reach comparable to that of the external fields. Shifting the composition from tellurium-rich to selenium-rich moved the absorption resonance from approximately 40 meV to 55 meV solely through changes in the bandgap and effective mass, without any external control. The accompanying drop in peak magnitude reflected the heavier effective mass suppressing the oscillator strength. This presents a design trade-off between peak position and peak intensity

that device engineers would need to negotiate depending on the target application. Layered on top of this compositional baseline, the electric field redshifted the resonance and enhanced $\chi^{(2)}$ and $\chi^{(3)}$ nearly twofold at 80 kV/cm. The magnetic field, by contrast, repositioned the resonance upward without meaningfully changing its strength. These two fields thus operate as largely orthogonal spectral controls, which is a useful property when attempting to lock a device onto a specific operating wavelength.

The thermodynamic findings for the chalcogenide system revealed one particularly notable feature: the insensitivity of entropy to the applied electric field. Across the full temperature range up to 1200 K, entropy curves computed at different field strengths were nearly indistinguishable. This behaviour traces to the Stark effect displacing all eigenenergies by similar amounts and leaving their relative spacings intact, so that the statistical occupation of the levels barely changes. Practically, this decoupling means that electrical tuning of the optical response does not carry a thermal stability penalty a significant advantage for devices that must operate reliably over a range of ambient conditions. The magnetocaloric results add further interests, the isothermal entropy change switched sign somewhere between 400 K and 600 K, marking a crossover from conventional to inverse magnetocaloric response. Such a crossover is a fingerprint of the discrete level structure in a confined system.

The MoS_2 study brought pressure to the foreground in a way that the chalcogenide study did not. Over a 0–3 GPa sweep, pressure produced spectral blueshifts larger than those from all other perturbations combined. At the same time, it drove $\chi^{(2)}$ down by nearly 90% and $\chi^{(3)}$ down by over 95%. The underlying mechanism is wavefunction localisation. Increasing pressure compresses the crystal lattice, widens the bandgap, raises the effective mass, and deepens the barrier heights. Each subband wavefunction becomes more tightly confined within its own sub-well, breaking the spatial overlaps that sustain the nonlinear dipole products. Temperature moved in the opposite direction. Despite producing the smallest spectral shifts of any perturbation less than 1 meV from 200 K to 500 K it was the only one that consistently strengthened both $\chi^{(2)}$ and $\chi^{(3)}$. The reason is that wavefunction spreading at higher temperatures improves intersubband coupling. This means that a MoS_2 asymmetric well actually becomes a more efficient frequency converter as it warms up, a result that runs counter to the usual expectation and would not have emerged from single-parameter studies.

Across both material systems, the central finding is that composition and external perturbations interact in ways that single-parameter studies cannot predict. The opposing actions of electric and magnetic fields, the dominance of pressure in the MoS_2 thermodynamic response, and the thermal enhancement of nonlinearity are all features that emerge only when the full parameter space is sampled. Both $As_2(Se_xTe_{1-x})_3$ and MoS_2 demonstrated sufficient tunability across the mid-infrared and terahertz regimes to be credible candidates for next-generation electro-optic and thermo-optic devices. The framework developed here provides a direct route to optimising their performance.

7.2 Future Scope

The results of this dissertation point toward several directions that would be worth pursuing next. The one that connects most directly to the existing work is a study of the mechanical properties of both material systems within the same quantum well geometries used here. Hydrostatic pressure was already shown to be the dominant perturbation in the MoS_2 system, and a logical extension is to move from isotropic pressure to directional strain. Uniaxial strain along the growth direction and biaxial in-plane strain are not equivalent in their effects on the subband structure, and mapping that anisotropy would connect the idealized pressure model used here to the realistic stress states that arise in substrate-mounted or flexible device configurations. For $As_2(Se_xTe_{1-x})_3$, the composition dependence of the elastic constants in a confined geometry has not been reported anywhere in the literature. Understanding how mechanical stiffness evolves with x, and how strain-induced effective mass renormalization feeds back into the optical properties, would be a direct and meaningful continuation of the composition-dependent results in Chapter 3.

Lastly, experimental fabrication and characterization of these structures remains the most important long-term validation step. Nano indentation and Brillouin light scattering on $As_2(Se_xTe_{1-x})_3$ films across the composition range, and atomic force microscopy based mechanical testing on suspended MoS_2 asymmetric well membranes, would provide direct tests of both the optical predictions made here and any future mechanical calculations. That combination of computational prediction and experimental verification would complete what this dissertation has started.

References

[1] S. Adachi, “Band gaps and refractive indices of AlGaAs, InGaP, and AlInP,” *J. Appl. Phys.*, vol. 66, no. 12, pp. 6030–6034, Dec. 1989. DOI: 10.1063/1.343545

[2] D. Ahn and S. L. Chuang, “Calculation of linear and nonlinear intersubband optical absorption in quantum wells,” *IEEE J. Quantum Electron.*, vol. 23, no. 12, pp. 2196–2204, 1987. DOI: 10.1109/JQE.1987.1073466

[3] E. B. Al, E. Kasapoglu, and F. Ungan, “Combined electric and magnetic field effects on the nonlinear optical properties of a quantum well,” *Eur. Phys. J. Plus*, vol. 137, p. 466, 2022. DOI: 10.1140/epjp/s13360-022-02702-x

[4] E. B. Al, E. Kasapoglu, and F. Ungan, “Dynamics of nonlinear optical rectification, second, and third harmonic generation in asymmetric triangular double quantum wells due to static electric and magnetic fields,” *Eur. Phys. J. Plus*, vol. 137, p. 466, 2022. DOI: 10.1140/epjp/s13360-022-02702-x (duplicate of [3])

[5] S. Arora, Y. Gupta, P. Khosla, Priyanka, and R. Sharma, “Impact of impurity on mean energy, heat capacity, free energy, entropy and magnetocaloric effect of $Ga_{1-x}Al_xAs$ quantum wire,” *J. Low Temp. Phys.*, vol. 212, no. 1, pp. 54–68, 2023. DOI: 10.1007/s10909-023-02995-x

[6] S. A. Azizova et al., “An investigation of structural, thermo-physical, and photoelectric properties of glassy As_2Se_3–TI_2Te_3 alloys,” *Mod. Phys. Lett. B*, vol. 38, no. 25, p. 2450232, Sep. 2024. DOI: 10.1142/S0217984924502327

[7] G. Bastard, *Wave Mechanics Applied to Semiconductor Heterostructures*. Les Ulis, France: Les Éditions de Physique, 1988.

[8] M. Behera and R. Naik, “Optical properties change in laser-induced Te/As_2Se_3 chalcogenide thin films,” *Appl. Phys. A*, vol. 122, p. 913, 2016. DOI: 10.1007/s00339-016-0451-7

[9] A. Bilekkaya, Ş. Aktaş, S. E. Okan, and F. K. Boz, “Electric and magnetic field effects on the binding energy of a hydrogenic impurity in quantum well wires with different shapes,” *Superlattices Microstruct.*, vol. 44, pp. 96–105, 2008. DOI: 10.1016/j.spmi.2008.02.010

[10] A. Boda and A. Chatterjee, “Effect of Magnetic Field on Thermodynamic Properties of GaAs Quantum Dot,” *Appl. Phys. Res.*, 2022. DOI: 10.5539/apr.v14n2p1

[11] B. Boyacioglu and A. Chatterjee, “Heat capacity and entropy of a GaAs quantum dot with Gaussian confinement,” *J. Appl. Phys.*, vol. 112, no. 8, p. 083514, Oct. 2012. DOI: 10.1063/1.4759236

[12] T. B. Boykin, G. Klimeck, and F. Oyafuso, “Valence band effective-mass expressions in the $sp^3d^5s^*$ empirical tight-binding model applied to a Si and Ge parametrization,” *Phys. Rev. B*, vol. 69, p. 115201, 2004. DOI: 10.1103/PhysRevB.69.115201

[13] D. Brandová, T. Wágner, M. Vlček, and M. Frumar, "Crystallization kinetics of $(As_2Se_3)_{100-x}(As_2Te_3)_x$ glasses," *J. Am. Ceram. Soc.*, vol. 101, no. 11, pp. 4945–4954, Nov. 2018. DOI: 10.1111/jace.15735

[14] L. Brey, N. F. Johnson, and B. I. Halperin, "Optical and magneto-optical absorption in parabolic quantum wells," *Phys. Rev. B*, vol. 40, pp. 10647–10649, 1989. DOI: 10.1103/PhysRevB.40.10647

[15] B. Brunetti, V. Piacente, and P. Scardala, "Torsion vapor pressures and sublimation enthalpies of arsenic triselenide and tritelluride," *J. Chem. Eng. Data*, vol. 52, no. 1, pp. 24–29, Jan. 2007. DOI: 10.1021/je060235s

[16] F. Capasso, C. Gmachl, D. L. Sivco, and A. Y. Cho, "Quantum cascade lasers," *Phys. Today*, vol. 55, no. 5, pp. 34–40, 2002. DOI: 10.1063/1.1485582

[17] J. D. Castaño-Yepes, D. A. Amor-Quiroz, C. F. Ramirez-Gutierrez, and E. A. Gomez, "Impact of a topological defect and Rashba spin-orbit interaction on the thermo-magnetic and optical properties of a 2D semiconductor quantum dot with Gaussian confinement," *Physica E*, vol. 109, pp. 59–67, May 2019. DOI: 10.1016/j.physe.2019.01.007

[18] R. Chaurasiya, S. Dahiya, and R. Sharma, "A study of confined Stark effect, hydrostatic pressure and temperature on nonlinear optical properties in 1D $Ga_xAl_{1-x}As/GaAs/Ga_xAl_{1-x}As$ quantum dots under a finite square well potential," *Nanosystems: Phys. Chem. Math.*, vol. 14, no. 1, pp. 44–53, 2023. DOI: 10.17586/2220-8054-2023-14-1-44-53

[19] B. Chen, K. X. Guo, R. Z. Wang, Z. H. Zhang, and Z. L. Liu, "Intersubband optical absorption and refractive index changes in parabolic quantum wells: effects of applied electric fields," *Solid State Commun.*, vol. 149, pp. 310–314, 2009. DOI: 10.1016/j.ssc.2008.11.016

[20] Y.-T. Cheng, Z. Li, H. Zhang, and A. S. Krishnamoorthy, "Bonding Nature and Optical Properties of As_2Te_3 Phase-Change Material," *Phys. Status Solidi RRL*, vol. 16, p. 2100626, 2022. DOI: 10.1002/pssr.202100626

[21] C. T. Chou, P. K. Banerjee, and E. M. Logothetis, "Transport properties of amorphous As_2Se_3-As_2Te_3 system," *J. Phys. C: Solid State Phys.*, vol. 6, no. 1, pp. 133–140, Jan. 1973. DOI: 10.1088/0022-3719/6/1/018

[22] COMSOL Multiphysics®, *Semiconductor Module User's Guide*, Version 6.0. COMSOL AB, Stockholm, Sweden, 2023. [Online]. Available: https://www.comsol.com

[23] S. Dahiya, R. Chaurasiya, and R. Sharma, "Nonlinear optical properties in 1D GaAlAs/GaAs quantum dot under electric field, hydrostatic pressure and temperature using COMSOL," 2023. (Preprint / internal report)

[24] S. Dahiya, S. Lahon, and R. Sharma, "Tuning the nonlinear optical properties of a 1D excitonic GaAs quantum dot system under a semi parabolic potential with a detailed comparison with the experimental results: interplay of hydrostatic pressure and temperature," *Nanosystems: Phys. Chem. Math.*, vol. 15, no. 5, pp. 632–642, 2024. DOI: 10.17586/2220-8054-2024-15-5-632-642

[25] H. Dakhlaoui, "Temperature and pressure dependence of nonlinear optical properties in an asymmetric triple quantum well," *Eur. Phys. J. Plus*, vol. 139, 2024. DOI: 10.1140/epjp/s13360-024-04956-z

[26] H. Dakhlaoui, M. Sayrac, F. Ungan, and L. M. Pérez, "Nonlinear optical properties in a triple quantum well under electric and magnetic fields," *Results Phys.*, vol. 20, art. no. 103706, 2021. DOI: 10.1016/j.rinp.2020.103706

[27] B. Donfack and A. J. Fotue, "Effects of spin orbit interaction (SOI) on the thermodynamic properties of a quantum pseudodot," *J. Low Temp. Phys.*, vol. 204, pp. 206–222, Aug. 2021. DOI: 10.1007/s10909-021-02602-x

[28] C. O. Edet et al., "Thermomagnetic Properties with Magnetic and Aharonov-Bohm Fields," *Mathematics*, vol. 10, p. 2824, 2022. DOI: 10.3390/math10152824

[29] J. T. Edmond, "Electronic conduction in As_2Se_3, As_2Se_2Te and similar materials," *Br. J. Appl. Phys.*, vol. 17, no. 7, pp. 979–989, Jul. 1966. DOI: 10.1088/0508-3443/17/7/315

[30] M. M. Fejer, S. J. B. Yoo, R. L. Byer, A. Harwit, and J. S. Harris, "Observation of extremely large quadratic susceptibility at 9.6–10.8 μm in electric-field-biased AlGaAs quantum wells," *Phys. Rev. Lett.*, vol. 62, pp. 1041–1044, 1989. DOI: 10.1103/PhysRevLett.62.1041

[31] X. Gai et al., "Nonlinear characterization of GeSbS chalcogenide glass waveguides," *Sci. Rep.*, vol. 6, p. 39234, 2016. DOI: 10.1038/srep39234

[32] A. Gharaati and R. Khordad, "Superlattices and Microstructures," vol. 48, no. 3, pp. 276–283, Sep. 2010. DOI: 10.1016/j.spmi.2010.06.008

[33] D. Grundler, "Large Rashba splitting in InAs quantum wells due to electron wave function penetration into the barrier layers," *Phys. Rev. Lett.*, vol. 84, no. 26, pp. 6074–6077, Jun. 2000. DOI: 10.1103/PhysRevLett.84.6074

[34] G. Q. Guo, K. C. Liu, and S. S. Li, "Third order nonlinear optical susceptibility in quantum wells," *Appl. Phys. Lett.*, vol. 62, no. 12, pp. 1316–1318, 1993. DOI: 10.1063/1.108694

[35] Y. Gupta, P. Khosla, S. Arora, Priyanka, and R. Sharma, "Thermodynamic Properties of Conical Quantum Dot Modulated by External Fields and Rashba Spin–Orbit Interaction," *J. Low Temp. Phys.*, vol. 213, pp. 251–263, 2023. DOI: 10.1007/s10909-023-03003-y

[36] M. K. Gurnick and T. A. DeTemple, "Synthetic nonlinear semiconductors," *IEEE J. Quantum Electron.*, vol. 19, pp. 791–794, 1983. DOI: 10.1109/JQE.1983.1071930

[37] A. Haghighatzadeh, A. Attarzadeh, A. Salman Durmuslar, E. B. Al, and F. Ungan, "Modeling of electronic spectra and optical responses of a semiconductor AlGaAs/GaAs quantum well with three-step barriers: the role of external perturbations and impurity," *Eur. Phys. J. Plus*, vol. 139, art. no. 353, 2024. DOI: 10.1140/epjp/s13360-024-05165-4

[38] C.-H. Ho, "Electronic structure and optical property of $As_2(Te_{1-x}S_x)_3$ and $As_2(Te_{1-x}Se_x)_3$ crystals," *J. Alloys Compd.*, vol. 509, pp. 7198–7204, 2011. DOI: 10.1016/j.jallcom.2011.04.061

[39] P. Hosseinpour, "Effect of Gaussian impurity parameters on the valence and conduction subbands and thermodynamic quantities in a doped quantum wire," *Solid State Commun.*, vol. 322, p. 114061, Dec. 2020. DOI: 10.1016/j.ssc.2020.114061

[40] P. Hosseinpour, "The role of Rashba spin-orbit interaction and external fields in the thermal properties of a doped quantum dot with Gaussian impurity," *Physica B*, vol. 593, p. 412259, Sep. 2020. DOI: 10.1016/j.physb.2020.412259

[41] H.-X. Jiang and J. Lin, "Intersubband transitions in semiconductor quantum wells: Selection rules and polarization dependence," *Phys. Rev. B*, vol. 40, pp. 10025–10028, 1989. DOI: 10.1103/PhysRevB.40.10025

[42] M. J. Karimi and A. Keshavarz, "Second harmonic generation in asymmetric quantum wells under simultaneous electric and magnetic fields," *Physica E*, vol. 44, pp. 1900–1904, 2012. DOI: 10.1016/j.physe.2012.05.009

[43] J. Kasapoglu, H. Sari, I. Sökmen, and U. Yesilgul, "Effects of applied external fields on the nonlinear optical rectification, second, and third-harmonic generation in an asymmetrical semi-exponential quantum well," *Opt. Quantum Electron.*, vol. 54, p. 27, 2022. DOI: 10.1007/s11082-021-03425-6

[44] M. A. Khan, S. Ahmed, and T. Das, "Design and simulation of quantum well infrared photodetectors for optoelectronic applications," *Results in Engineering*, vol. 25, p. 106589, 2025. DOI: 10.1016/j.rineng.2025.106589

[45] R. Khordad, "Optical properties of quantum wires: Rashba effect and external magnetic field," *J. Lumin.*, vol. 134, pp. 201–207, Feb. 2013. DOI: 10.1016/j.jlumin.2012.09.012

[46] R. Khordad, "Study of Specific Heat of Quantum Pseudodot Under Magnetic Field," *Int. J. Thermophys.*, vol. 34, p. 1148, 2013. DOI: 10.1007/s10765-013-1480-6

[47] R. Khordad, "Thermodynamical properties of triangular quantum wires: entropy, specific heat, and internal energy," *Continuum Mech. Thermodyn.*, vol. 28, pp. 947–956, 2016. DOI: 10.1007/s00161-015-0429-2

[48] R. Khordad, A. Firoozi, and H. R. R. Sedehi, "Simultaneous Effects of Temperature and Pressure on Entropy and Specific Heat of a 3D Quantum Wire: Tsallis Formalism," *J. Low Temp. Phys.*, vol. 202, p. 185, 2020. DOI: 10.1007/s10909-020-02537-7

[49] R. Khordad and B. Mirhosseini, "Thermodynamic properties of a GaAs quantum dot with an effective-parabolic potential: Theory and simulation," *J. Low Temp. Phys.*, vol. 197, no. 1–2, pp. 95–119, Oct. 2019. DOI: 10.1007/s10909-019-02218-2

[50] R. Khordad and H. R. Rastegar Sedehi, "Low temperature behavior of thermodynamic properties of 1D quantum wire under the Rashba spin-orbit interaction and magnetic field," *Solid State Commun.*, vol. 269, pp. 118–125, Jan. 2018. DOI: 10.1016/j.ssc.2017.10.009

[51] R. Khordad and H. R. Rastegar Sedehi, "Thermodynamic Properties of a Double Ring-Shaped Quantum Dot at Low and High Temperatures," *J. Low Temp. Phys.*, vol. 190, pp. 200–212, 2018. DOI: 10.1007/s10909-017-1831-x

[52] R. Khordad, H. R. R. Sedehi, and M. Sharifzadeh, "Susceptibility, Entropy and Specific Heat of Quantum Rings in Monolayer Graphene," *J. Comput. Electron.*, vol. 21, p. 422, 2022. DOI: 10.1007/s10825-022-01870-8

[53] P. Khosla, S. Arora, Y. Gupta, Priyanka, and R. Sharma, "Hydrostatic Pressure Effect on the Thermodynamic Properties of Quantum Wire Under a Crossed Electromagnetic Field," *J. Low Temp. Phys.*, vol. 213, pp. 92–106, 2023. DOI: 10.1007/s10909-023-02992-0

[54] Y. Khoshbakht, R. Khordad, and H. R. Rastegar Sedehi, "Magnetic and thermodynamic properties of a nanowire with Rashba spin-orbit interaction," *J. Low Temp. Phys.*, vol. 202, no. 1–2, pp. 59–75, Jan. 2021. DOI: 10.1007/s10909-020-02550-w

[55] M. Kucur and İ. A. Ulutaş, "Effect of Temperature on Magnetic Susceptibility and Thermodynamic Properties of Asymmetric Quantum Dot in Tilted Magnetic Field," *Mod. Phys. Lett. B*, vol. 29, p. 1550127, 2015. DOI: 10.1142/S0217984915501278

[56] J. H. Lee, Y. K. Lee, D. W. Lee, and J. Y. Lee, "Composition-dependent bandgap and transition energies in $As_2(Te_{1-x}Se_x)_3$ and $As_2(Te_{1-x}S_x)_3$ systems," *J. Alloys Compd.*, vol. 424, no. 1–2, pp. 123–128, Nov. 2006. DOI: 10.1016/j.jallcom.2005.12.061

[57] D. Liang and X. P. A. Gao, "Strong tuning of Rashba spin-orbit interaction in single InAs nanowires," *Nano Lett.*, vol. 12, no. 6, pp. 3263–3267, Jun. 2012. DOI: 10.1021/nl3011397

[58] Y. Liu, X. Zhang, and J. Wang, "Spin–orbit coupling, electric field, and strain effects on MoS_2: A review," *Nanomaterials*, vol. 15, no. 14, p. 1100, 2025. DOI: 10.3390/nano15141100

[59] X. Lu et al., "The nonlinear second harmonic generation and third harmonic generation in GaAs/GaAlAs exponentially confined quantum well: Electric and magnetic field effects," *Superlattices Microstruct.*, vol. 171, p. 107071, 2022. DOI: 10.1016/j.spmi.2022.107071

[60] S. Maimon et al., "Intersubband transitions in GaN/AlN quantum wells grown on GaN substrates with metal organic vapor phase epitaxy," *Appl. Phys. Lett.*, vol. 76, pp. 1997–1999, 2000. DOI: 10.1063/1.126229

[61] D. A. B. Miller et al., "Band-edge electroabsorption in quantum well structures: the quantum-confined Stark effect," *Phys. Rev. Lett.*, vol. 53, pp. 2173–2176, 1984. DOI: 10.1103/PhysRevLett.53.2173

[62] D. A. B. Miller, D. S. Chemla, T. C. Damen, A. C. Gossard, W. Wiegmann, T. H. Wood, and C. A. Burrus, "Electric field dependence of optical absorption near the band gap of quantum-well structures," *Phys. Rev. B*, vol. 32, no. 2, pp. 1043–1060, Jul. 1985. DOI: 10.1103/PhysRevB.32.1043

[63] M. H. Mohammed et al., "Optical properties of thin films of system $(As_2Se_3)_{80-x}(As_2Te_3)_x(SnTe)_{20}$ prepared by PLD," *J. Non-Cryst. Solids*, vol. 355, no. 37–42, pp. 2222–2226, 2009. DOI: 10.1016/j.jnoncrysol.2009.07.028

[64] Mona, Akash, Priyanka, and R. Sharma, "Dependence of Matrix Elements on Hydrostatic Pressure and Temperature," *J. Phys.: Conf. Ser.*, vol. 2426, art. no. 012058, 2023. DOI: 10.1088/1742-6596/2426/1/012058

[65] R. A. Morrow and K. R. Brownstein, "Model effective-mass Hamiltonians for abrupt heterojunctions and the associated wave-function-matching conditions," *Phys. Rev. B*, vol. 30, pp. 678–680, 1984. DOI: 10.1103/PhysRevB.30.678

[66] B. Mortazavi, F. Shojaei, M. Azizi, T. Rabczuk, X. Zhuang, "As_2S_3, As_2Se_3 and As_2Te_3 nanosheets: Superstretchable semiconductors with anisotropic carrier mobilities and optical properties," *J. Mater. Chem. C*, vol. 8, pp. 2400–2410, 2020. DOI: 10.1039/C9TC05904K

[67] A. K. M. Newaz et al., "Electrical control of optical properties of monolayer MoS_2," arXiv preprint arXiv:1211.0341, 2012.

[68] T. T. Nguyen, T. T. T. Vu, T. T. P. Nguyen, and H. V. Phuc, "Hydrostatic pressure effect on the electronic and optical properties of MoS_2 monolayer," *RSC Adv.*, vol. 10, pp. 8532–8540, 2020. DOI: 10.1039/C9RA10889K

[69] E. C. Niculescu, L. M. Burileanu, and A. Radu, "Second and third harmonic generation in asymmetric quantum wells under electric and pressure fields," *Eur. Phys. J. B*, vol. 86, no. 122, 2013. DOI: 10.1140/epjb/e2013-30994-5

[70] J. H. Oh, K. J. Chang, G. Ihm, and S. J. Lee, "Heat capacity of quantum wires and dots under magnetic field," *J. Korean Phys. Soc.*, vol. 28, no. 1, pp. 132–136, Feb. 1995.

[71] O. Olendski, "Comparative analysis of electric field influence on quantum wells with different boundary conditions. II. Thermodynamic properties," arXiv preprint arXiv:1502.03007, 2015.

[72] O. Olendski, "Thermodynamic properties of a one-dimensional quantum well: Influence of the electric field," *Ann. Phys.*, vol. 527, no. 4, pp. 296–310, Apr. 2015. DOI: 10.1002/andp.201400240

[73] M. Ortolani, L. Baldassarre, E. Giovine, et al., "Second harmonic generation in germanium quantum wells for nonlinear silicon photonics," *Phys. Rev. B*, vol. 103, p. 125301, 2021. DOI: 10.1103/PhysRevB.103.125301

[74] S. Pandey, S. K. Pandey, and V. K. Jindal, "Varshni parameters for monolayer MoS_2," *Phys. Rev. B*, vol. 98, art. no. 045311, 2018. DOI: 10.1103/PhysRevB.98.045311

[75] V. Parchanski, B. Frumarova, M. Frumar, M. Hrdlicka, and M. Vlček, "Optical properties and photoinduced phenomena in glasses and thin films of system As_2Se_3–As_2Te_3–SnTe," *J. Optoelectron. Adv. Mater.*, vol. 14, no. 1–2, pp. 150–156, Feb. 2012.

[76] V. Parchanski, P. Němec, I. Gregora, and V. Vorlíček, "Optical properties of thin films of system $(As_2Se_3)_{80-x}(As_2Te_3)_x(SnTe)_{20}$ prepared by pulsed laser deposition," *J. Non-Cryst. Solids*, vol. 355, pp. 2225–2229, 2009. DOI: 10.1016/j.jnoncrysol.2009.07.028

[77] T. G. Pedersen, "An exact and compact formula for the optical intersubband response of finite-barrier quantum wells, wires and dots," *Solid State Commun.*, vol. 341, p. 114553, 2022. DOI: 10.1016/j.ssc.2021.114553

[78] Priyanka, S. Arora, Y. Gupta, P. Khosla, and R. Sharma, "Impact of impurity on the mean energy, heat capacity, free energy, entropy and magnetocaloric effect of $Ga_{1-x}Al_xAs$ quantum wire," *J. Low Temp. Phys.*, vol. 200, pp. 1–16, 2020. DOI: 10.1007/s10909-020-02345-7

[79] Priyanka and R. Sharma, "Impact of impurity on the non-linear and linear optical properties of $In_xGa_{1-x}As$ quantum dot," *Solid State Commun.*, vol. 338, p. 115155, 2021. DOI: 10.1016/j.ssc.2021.115155

[80] Priyanka and R. Sharma, "Impurity modulated physical and transport properties in a $In_xGa_{1-x}As$ double quantum wire," *Physica E*, vol. 154, p. 115139, 2023. DOI: 10.1016/j.physe.2023.115139

[81] Priyanka and R. Sharma, "Impurity-modulated physical and transport properties in a $In_xGa_{1-x}As$ double quantum wire," *Micro and Nanostructures*, vol. 154, p. 115139, 2024. DOI: 10.1016/j.micrna.2024.207876 (duplicate of [80])

[82] Priyanka, R. Sharma, and M. Kumar, "Effects of impurity factor on the physical and transport properties for $Ga_{1-x}Al_xAs$ quantum wire in the presence of Rashba spin–orbit interaction," *Physica B*, vol. 629, p. 413649, 2022. DOI: 10.1016/j.physb.2022.413649

[83] Priyanka, R. Sharma, M. Kumar, and P. Kumar, "Hydrogenic impurity effect on the optical properties of $Ga_{1-x}Al_xAs$ quantum wire under terahertz field," *Micro and Nanostructures*, vol. 173, p. 207451, 2024. DOI: 10.1016/j.micrna.2024.207451

[84] Priyanka and R. Sharma, "Thermodynamic properties of $In_xGa_{1-x}N$ double quantum wire in the presence of impurity and Rashba spin-orbit interaction," *Physica B*, vol. 692, p. 416305, Nov. 2024. DOI: 10.1016/j.physb.2024.416305

[85] H. R. Rastegar Sedehi, "Magnetocaloric effect in Rashba spin-orbit coupling and Zeeman splitting of a narrow nanowire quantum dot," *Eur. Phys. J. Plus*, vol. 136, no. 5, p. 514, May 2021. DOI: 10.1140/epjp/s13360-021-01519-4

[86] H. R. Rastegar Sedehi and R. Khordad, "Magnetocaloric effect magnetic susceptibility and specific heat of tuned quantum dot/ring systems," *Physica E*, vol. 134, p. 114886, Oct. 2021. DOI: 10.1016/j.physe.2021.114886

[87] A. H. Reshak and S. Auluck, "Optical properties of chalcogenide glasses for infrared applications," *Optik*, vol. 124, no. 17, pp. 3045–3050, 2013. DOI: 10.1016/j.ijleo.2013.05.169

[88] J. Rodríguez-Magdaleno et al., "Effect of the magnetic field on the nonlinear optical rectification and second and third harmonic generation in double δ-doped GaAs quantum wells," *Physica B*, vol. 525, pp. 30–42, 2017. DOI: 10.1016/j.physb.2017.08.049

[89] A. Rostami and R. Asgari, "Electronic structure of MoS_2 monolayer under electric and magnetic fields," *Phys. Rev. B*, vol. 88, art. no. 085440, 2013. DOI: 10.1103/PhysRevB.88.085440

[90] H. Sari, E. Kasapoglu, I. Sökmen, and M. E. Mora-Ramos, "Nonlinear optical rectification and the second and third harmonic generation in Pöschl–Teller quantum well under the intense laser field," *Eur. Phys. J. B*, vol. 85, p. 31, 2012. DOI: 10.1140/epjb/e2011-20479-6

[91] H. Sari, F. Ungan, U. Yesilgul, and I. Sökmen, "Intersubband optical absorption in step quantum well structures," *J. Appl. Phys.*, vol. 105, p. 023109, 2009. DOI: 10.1063/1.3065076

[92] H. Sari, U. Yesilgul, and I. Sökmen, "Theoretical investigation of intersubband optical absorption in step quantum well structures," *Superlattices Microstruct.*, vol. 52, no. 3, pp. 391–399, 2012. DOI: 10.1016/j.spmi.2012.03.008

[93] M. Servatkhah, R. Khordad, A. Firoozi, H. R. Rastegar Sedehi, and A. Mohammadi, "Low temperature behavior of entropy and specific heat of a three dimensional quantum wire: Shannon and Tsallis entropies," *Eur. Phys. J. B*, vol. 93, art. no. 111, 2020. DOI: 10.1140/epjb/e2020-10034-5

[94] Y. R. Shen, *Principles of Nonlinear Optics*. New York, NY, USA: Wiley, 1984.

[95] P. K. Shukla and S. K. Tripathy, "Optical properties of step quantum wells for mid-infrared photodetector applications," *Physica E*, vol. 156, p. 116527, 2026. DOI: 10.1016/j.physe.2026.116527

[96] M. Solaimani, "Specific heat of quantum ring in the presence of a quantum well," *J. Nano-Electron. Phys.*, vol. 10, no. 6, p. 06006, Dec. 2018. DOI: 10.21272/jnep.10(6).06006

[97] D. M. Sullivan and D. S. Citrin, "Time-domain simulation of quantum systems," *J. Appl. Phys.*, vol. 97, no. 10, p. 104305, May 2005. DOI: 10.1063/1.1896091

[98] "Thermal effects on glass $As_2Se_3 \cdot As_2Te_3$," *J. Therm. Anal. Calorim.*, vol. 34, pp. 93–98, 1988. DOI: 10.1007/BF01913356

[99] "Thermodynamic properties of As_2Te_3 from 450 to 900 K," *J. Chem. Thermodyn.*, vol. 3, no. 6, pp. 821–828, Nov. 1971. DOI: 10.1016/S0021-9614(71)80007-X

[100] "Thermoelectric power of AsSeTe glasses," *J. Non-Cryst. Solids*, vol. 34, no. 1, pp. 53–62, Aug. 1979. DOI: 10.1016/0022-3093(79)90007-3

[101] C. V. Thompson, "Electronic properties of glassy As_2Te_3," *J. Non-Cryst. Solids*, vol. 8–10, pp. 628–634, 1972. DOI: 10.1016/0022-3093(72)90159-7

[102] S. Tongay et al., "Thermally driven crossover from indirect to direct bandgap in monolayer MoS_2," *Nano Lett.*, vol. 12, no. 11, pp. 5576–5580, 2012. DOI: 10.1021/nl302863w

[103] C. Tsallis, "Possible generalization of Boltzmann-Gibbs statistics," *J. Stat. Phys.*, vol. 52, no. 1–2, pp. 479–487, Jul. 1988. DOI: 10.1007/BF01016429

[104] F. Ungan, U. Yesilgul, E. B. Al, and M. E. Mora Ramos, "Magnetic field effect on the optical absorption and refractive index in a quantum well," *Optik*, vol. 181, pp. 179–185, 2019. DOI: 10.1016/j.ijleo.2018.12.112

[105] F. Ungan, U. Yesilgul, E. Kasapoglu, H. Sari, and I. Sökmen, "Effect of the magnetic field and intense laser field on the optical properties of a quantum well," *J. Lumin.*, vol. 132, pp. 1627–1631, 2012. DOI: 10.1016/j.jlumin.2012.01.016

[106] K. Ungan, M. E. Mora-Ramos, C. A. Duque, E. Kasapoglu, H. Sari, and I. Sökmen, "Nonlinear optical rectification and the second and third harmonic generation in asymmetric semi-parabolic quantum well: effects of intense laser field, electric and magnetic fields," *Physica E*, vol. 86, pp. 130–135, 2017. DOI: 10.1016/j.physe.2016.09.027

[107] Y. Wang and S. Dai, "Mid-infrared supercontinuum generation in chalcogenide glass fibers: a brief review," *PhotoniX*, vol. 2, p. 9, 2021. DOI: 10.1186/s43074-021-00031-3

[108] X. Wen, Z. He, Y. Li, and H. Chen, "Magnetic field tuned terahertz optical properties of MoS_2," *Nano Select*, vol. 2, pp. 234–242, 2021. DOI: 10.1002/nano.202000156

[109] W. Xie and Y. Chen, "Nonlinear optical properties in a quantum dot: impurity and confinement effects," *Superlattices Microstruct.*, vol. 50, pp. 691–700, 2011. DOI: 10.1016/j.spmi.2011.09.003

[110] C. Xiong et al., "Integrated nonlinear photonics with chalcogenide glasses: compositions, properties, applications, and roadmap," *Opt. Mater. Express*, vol. 15, no. 12, pp. 3210–3267, 2025. DOI: 10.1364/OME.545459

[111] N. Yahyaoui, A. Bouazra, and M. Said, "Impact of the applied electric field on the optical absorption coefficient in Ge/Si–Ge step quantum well," *Discover Applied Sciences*, vol. 7, p. 403, 2025. DOI: 10.1007/s42452-025-06685-z

[112] N. Yahyaoui et al., "Impact of the applied electric field on the optical absorption coefficient in $Ge/Si_{1-x}Ge_x$ step quantum well," *Discov. Appl. Sci.*, vol. 7, p. 403, 2025.

[113] M. Yamanishi and I. Suemune, "Comment on polarization dependent momentum matrix elements in quantum well lasers," *Jpn. J. Appl. Phys.*, vol. 23, p. L35, 1984. DOI: 10.1143/JJAP.23.L35

[114] "New insight into the electronic structure of a As_2Se_3," *Phys. Rev. B*, vol. 33, no. 4, pp. 1–12, Feb. 1986. DOI: 10.1103/PhysRevB.33.2615